# The Correction of Artefacts in an Imaging Detector used for Electron Spectroscopy

Thesis

submitted to

ABERYSWYTH UNIVERSITY

by

**Thomas Robert Chase MPhys. (Hons.) Aberystwyth**

**Aberystwyth University**

**in candidature for the degree of Master of Philosophy**

Department of Physics

Aberystwyth University

January 2009

Declaration

I hereby declare that this work has not already been accepted in substance for any degree, and is not being concurrently submitted in candidature for any degree.

Signed.......................................................(Candidate)

Date....................................................................

STATEMENT 1

This thesis is the result of my own investigations, except where otherwise stated.

Other sources are acknowledged by footnotes giving explicit references. A bibliography is appended.

Signed.......................................................(Candidate)

Date....................................................................

STATEMENT 2

I hereby give consent for my thesis, if accepted, to be available for photocopying and for inter-library loan, and for the title and summary to be made available to outside organisations,

Signed.......................................................(Candidate)

Date....................................................................

Abstract

This thesis covers the range of aberrations occurring when an electron counting imaging detector is placed at the focal plane of an electron energy analyser used for photoelectron spectroscopy.

The technique of photoelectron spectroscopy is introduced, showing how it may be used to characterise the surface layers of a sample. The nature of artefacts and aberrations observed in an electron energy analyser are discussed and consideration is given to different techniques and algorithms to correct a measured spectrum for these artefacts.

# Contents

# Chapter 1

# Introduction

Electron spectroscopy is a widely used method for studying materials. Electrons are excited by incident radiation and the collected electrons are energy-analysed to give spectra. The techniques are most commonly described by the source of excitation. For example, if electromagnetic radiation is used as the source of excitation, the techniques is known as Photoelectron Spectroscopy (PES). This is broken down into Ultraviolet photoelectron spectroscopy (UPS), X-ray photoelectron spectroscopy (XPS) [20], or Soft X-ray Photoelectron Emission Spectroscopy (SXPS). XPS is sometimes referred to as Electron Spectroscopy for Chemical Analysis (ESCA) and was first developed by Kai Siegabahn in 1957 [8] [25], for which he got a Nobel Prize. Electron-excited techniques include Auger Electron Spectroscopy (AES) and Electron energy loss spectroscopy (EELS).

In all cases, the incident energy must have sufficient energy to emit electrons and sufficient intensity to provide enough electrons for energy analysis. The efficient detection of the electrons is a major factor in determining the quality of the experiments that can be performed. In this thesis, the techniques applied are XPS and SXPS and the emphasis is on developing electron detection to extend, in particular, the application of the technique in the time domain to enable real-time measurements. In the following sections, the basics of the photoemission process are reviewed in the context of such experiments. Some discussion of the sources is also included.

## 1.1 Basic Process of Photoemission

Photoemission techniques by their nature need a vacuum environment and so the development of the techniques was only possible with advances in vacuum technology in the 1960s and 1970s. However, the photoelectric effect, where electrons are emitted from the surface of a solid irradiated with electromagnetic radiation was understood and demonstrated long before this [15], and was studied by Einstein, who gave the first description of the photoelectric effect as caused by quantum effects [11]. The basic photoemission process can be illus-

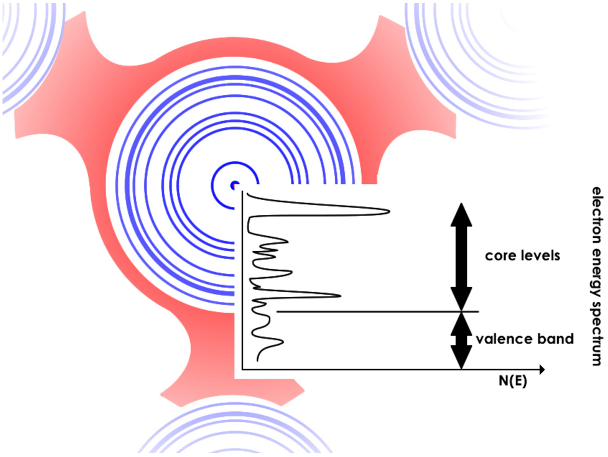

Figure 1.1: Schematic of photoelectron spectra in relation to electron energy levels in a solid.

trated qualitatively for an atom within a crystalline solid as shown in Figure 1.1. The core levels are atomic-like and these give rise to sharp peaks in the photoemission spectrum. The outer electrons that are involved in bonding in the solid are more delocalised and these give rise to broad bands (e.g. the valence band of a semiconductor). In Figure 1.1 a schematic spectrum is shown superimposed on the simple shell picture of energy levels associated with the central atom. The spectrum measures the energy distribution N(E) and so it is important to be able to correlate this with the energy levels of the electrons within the solid. The energy levels probed will depend on the incident photon energy.

If the solid is a compound material, the energy levels of the different elements are separated in the photoemission spectrum and so the technique can detect (and quantify) the elements present in the solid. Atoms of the same element in different chemical environments will also have different energy levels although the differences in energy will be less. The technique can also be made sensitive to these differences and hence can be used as a probe of chemical bonding in solids, for example in separating a metal from it's oxide.

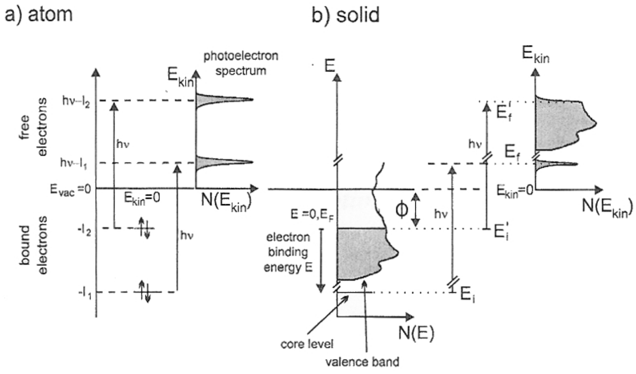

Figure 1.2: Photoelectron spectroscopy of: a) an atom, b) a metallic solid.

In Figure 1.2 [1] the relationship between the electron energy levels and the photoelectron spectrum is shown for a single atom and for a solid. Two levels are shown that have ionisation energies of $I_1$ and $I_2$. In the simplest picture, photoelectrons excited by photons of frequency $\nu$ will be emitted with kinetic energies given by equation 1.1:

$$E_{kin1} = h\nu - I_1 \tag{1.1}$$

$$E_{kin2} = h\nu - I_2 \tag{1.2}$$

The ionisation energy is referred to the vacuum level ($E_{vac} = 0$) and there is a direct correlation between kinetic and binding energies. Although this is a useful approximation, the energies will not in reality follow this simple picture since after ionisation, the atom has N-1 electrons and this will change the energy levels and the photoelectron energies usually have higher energies than predicted.

In Figure 1.2b, the energy level diagram for the photoemission process is shown for a metal with initial electron states $E_i$ and final states $E_f$. The binding energy for electrons in a metal, $E_b$, are usually referred to the Fermi level $E_f$ rather than the vacuum level. The Fermi level is defined as the highest occupied state for metals (at 0 K). For an insulator or a semiconductor, the Fermi level is not as clearly defined as it lies between the occupied and the unoccupied states (i.e. within the forbidden gap for a semiconductor).

As shown in figure 1.2b, the kinetic energy of electrons which are emitted from the metal in this simple model is given by Equation 1.3:

$$E_{kin} = h\nu - E_b - \mathit{\Phi} \tag{1.3}$$

where $\Phi$ is the work function of the crystal.

In this simple picture, the measured kinetic energy of the photoelectron is directly related to its binding energy in the solid and, if the work function is known, then the absolute binding energy is in principle measured.

## 1.2 Quantitative Description

A quantitative description of the photocurrent in PES is rather complex and depends on a variety of factors. However, the basic principles can be illustrated using the three step model which will be introduced briefly. The first step is photoexcitation into an unoccupied state, the second step is propagation through the solid to the surface and the third step is emission at the surface into the vacuum. The probability of emission is then the product of all three probabilities. In the photoelectron spectroscopy experiment, transmission and detection in the electron analyser must also be considered. The following sections summarise the steps from the absorption of the photon to emission into the vacuum:

### 1.2.1 Photoexcitation

The most important step in the model is the photoexcitation of an electron by a photon into an excited state. The number of electrons is assumed to be determined by equation 1.4:

$$N(E_h, h\nu) \sim \int D_i(E_i) D_f(E_i + h\nu) \left|M_{fi}\right|^2 dE_i \tag{1.4}$$

where $N$ is the number of photoexcited electrons $D_i$ is the local density of states of the initial state $D_f$ is the local density of states of the final state $M_{fi}$ is the matrix element describing the transition from initial to final state.

Equation 1.4 predicts that the number of photoelectrons depends not only on the density of states at the initial energy (occupied states) but also on the density of states at the final energy (empty states). This is important for low photon energies (UPS) but for higher photon energies the density of final states can be taken to be uniform and so the number of photons as a function of energy (N(E)) will reflect the density of initial states and this is the usual assumption for XPS and SXPS.

### 1.2.2 Electron Propagation: Mean free path

The second process in the emission of photoelectrons is propagation through the solid to the surface. During this process, electrons can lose energy in many ways and most electrons emerge with considerably lower energies as a result of inelastic scattering events. The photoelectron spectrum therefore does not consist only of peaks due to direct transitions given by equation 1.3, but also contains inelastic loss peaks and a large background of secondary electrons. The collective effect of all losses is most conveniently described by the mean free path of the photoelectron. In practical terms, this defines the effective sampling depth of the experiment - a feature that is both an advantage and a disadvantage of the technique. Since the inelastic losses will depend on the energy of the photoelectron, the mean free path is strongly dependent on energy as shown in figure 1.3.

The main causes of inelastic scattering are: electron-hole pair excitation, electron plasmon excitation, electron-phonon scattering and electron impurity scattering, all leading to different amounts of energy loss. Electrons are also likely to undergo multiple inelastic scattering before they reach the surface - these contribute to the featureless background. Energy losses for electron-hole excitation are in the range ∼eV (low energy UPS), plasmon excitations at ∼10-50eV (UPS and XPS), while phonon scattering with energies of ∼100 meV are the least important in XPS and SXPS.

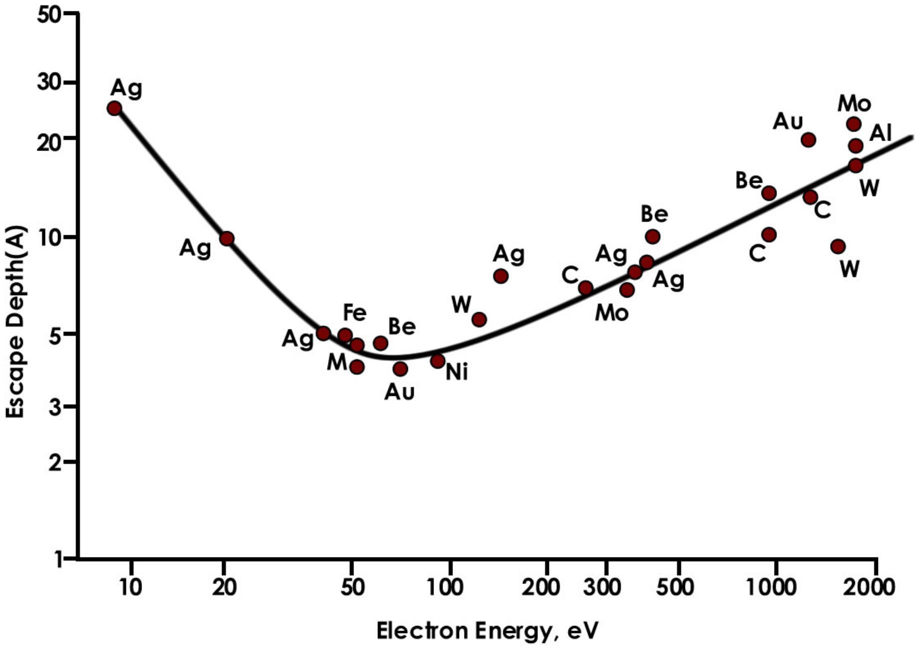

Figure 1.3: Inelastic mean free path for electrons with typical UPS and XPS energies

The penetration depth of UV and soft x-ray photons is much greater than the electron mean free path and so the sampling depth of UPS and XPS are determined by the mean free path. As seen in figure 1.3, the minimum of mean free path of an electron liberated from PES is around 0.5 nm and this occurs at around 50 eV [21]. Therefore, for maximum surface sensitivity, the electron energy must be chosen to be approximately this value. Such tuning is only possible with a variable photon energy such as provided by a synchrotron radiation source. For probing the bulk of materials, either very low energy or high energy sources can be used.

### 1.2.3 Emission at the Surface: the Work Function

The final stage of the photoemission process is emission from the surface. This is usually considered as a simple transmission function of an electron across an abrupt potential step. At the surface of a metal, the potential step is defined by the work function, while for a semiconductor, it is defined by the ionisation energy. An important consideration for photoemission experiments is the relative magnitude of the sample work function and that of the analyser. The lowest energy electrons emitted can only be detected if the work function of the analyser is less than that of the sample. The work function (or ionisation energy) can then be measured directly by the photoemission technique.

## 1.3 Photon Sources

### 1.3.1 UV Sources

Ultraviolet sources commonly used in laboratory experiments are usually based on the excitation, by electrons emitted from a filament, of noble gases and by far the most common is He. The discharge of He gives rise to two main lines: He I at 21.2 eV and He II at 40.8 eV. These energies are sufficient to ionise valence electrons in most solids and shallow core levels in some. The radiation can also be polarised and passed through a monochromator.

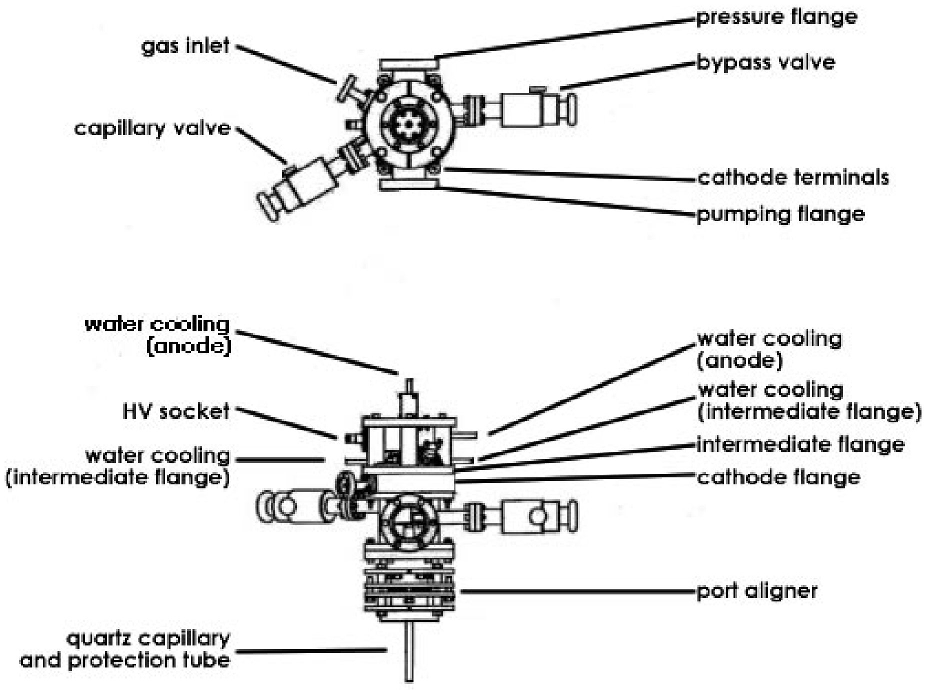

Figure 1.4: SPECS UVS 300 UV Lamp [26]

### 1.3.2 X-ray sources

Laboratory x-ray sources for XPS usually use electron impact on low Z metals such as Mg and Al. The electrons are emitted from a filament, and accelerated towards a target anode. The impact of the electrons on the target causes X-rays to be emitted. At Aberystwyth a Thermo VG XR3E2 twin-anode source is used. This has an anode coated on one side with aluminium, and magnesium on the other. Rotating the anode allows either side to be used as the target, depending on which energy X-rays are required. The two settings provide photon energies of 1486.6eV (Al K$\alpha$) and 1253.6eV (Mg K$\alpha$). The Mg source has line-width of $\sim$0.7eV whereas the Al source, when monochromatised, has a line-width of $\sim$0.2eV. The energy is sufficiently high to excite electrons from core levels in most elements and this enables the technique to be used for chemical composition. The energy resolution is sufficient for more detailed chemical analysis, for example in separating different oxidation states of the elements.

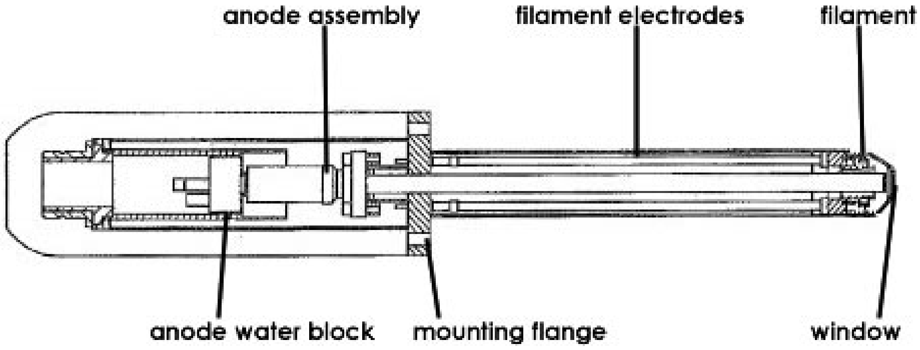

Figure 1.5: SPECS UVS XR3E2 twin anode X-ray source [27]

### 1.3.3 Synchrotron Radiation Sources

Synchrotron radiation sources have several advantages over laboratory sources. The main feature is the continuous range of tunable photon energies that allows the incident light to be changed to give the most suitable energy for the experiment. Synchrotron radiation is also more intense than laboratory sources offering several orders of magnitude increases in photon flux density. The radiation is also naturally polarised and collimated and covers an energy range extending from the infra-red to hard x-rays. The main disadvantage is the need for expensive accelerators and storage rings for their production and the need to transport the experimental apparatus to central facilities in limited time-slots.

All photoelectron spectroscopy experiments described in this thesis were carried out at the UK's Synchrotron Radiation Source (SRS) at the STFC Daresbury Laboratory, and this source is shown schematically in figure 1.6.

Electrons are generated in a filament source and initially accelerated in a

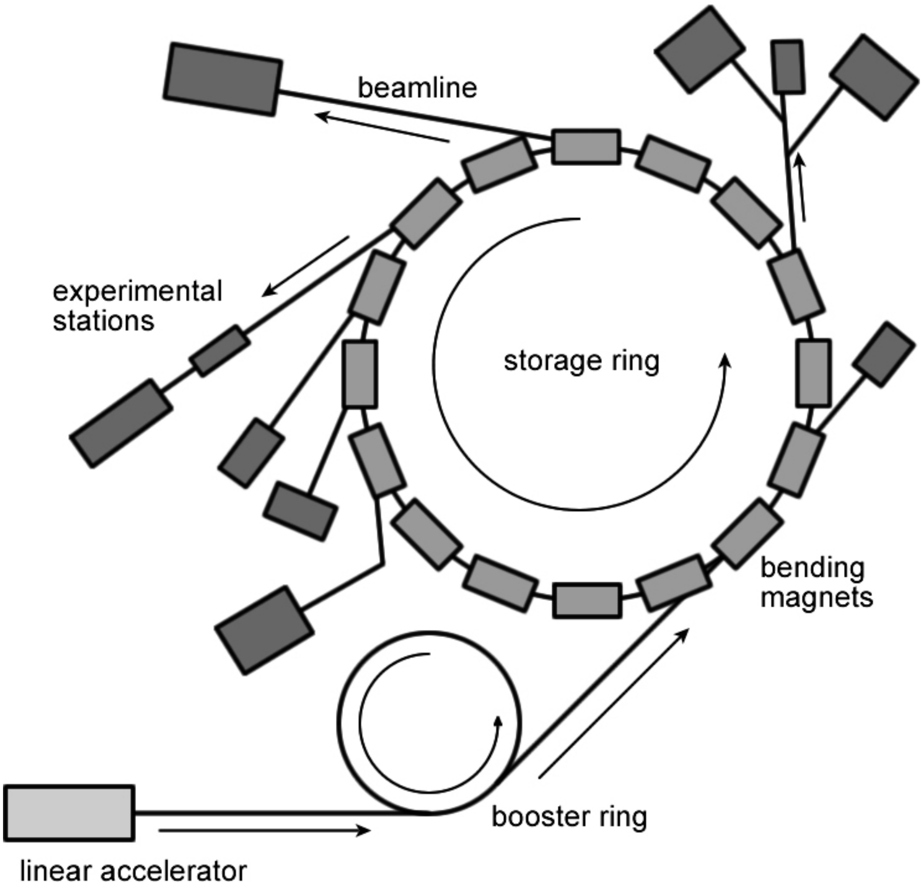

Figure 1.6: The synchrotron radiation source at the Daresbury Laboratory

linear accelerator up to an energy of 12 MeV. The next stage is acceleration in the booster synchrotron up to an energy of 600MeV. The electrons are finally injected into the main storage ring where the energy is increased to around 2GeV to provide a beam current of around 300mA. The storage ring has a diameter of 31m, made up of an array of 16 bending magnets that confine the electrons within the storage ring. Acceleration of the high energy electrons by the magnetic field results in the emission of electromagnetic radiation and since the electrons are moving with relativistic velocities, the effect of relativity is such that the synchrotron radiation (in the laboratory frame of reference) is emitted in a narrow cone along the direction of travel.

The experimental stations are located at each magnet at the end of long tubes along which the beams of radiation are emitted from the storage ring. These beamlines are equipped with optical components such as beam-splitters, slits, monochromators and mirrors to provide the required energy and profile of the beam for each experiment. The beamline used in this case was beamline 4.1, shown in figure 1.7.

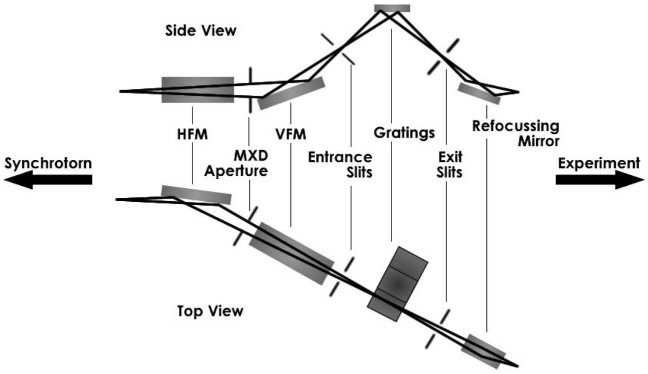

Figure 1.7: Beamline 4.1 at the Daresbury Laboratory

As shown in figure 1.7, the synchrotron radiation is collimated and focussed by the horizontal focussing mirror (HFM), an aperture, the vertical focussing mirror (VFM) and entrance and exit slits placed before and after the diffraction grating respectively. The diffraction grating unit has three interchangeable gratings.

## 1.4 Electron Energy Analysers

Photoelectrons emitted from a solid irradiated by UV or X-rays must be separated in energy and there are several methods available for achieving this.

Electron energy analysers usually use electrostatic fields for focusing and dispersing the electrons although magnetic fields can also be used in some cases. The most common analysers use a pair of charged hemispheres for the dispersion and cylindrical lenses for focusing. These are known as concentric hemispherical analysers, or CHAs. The basic design is shown in Figure 1.8. An analyser of this design was used in all of the experiments in this thesis.

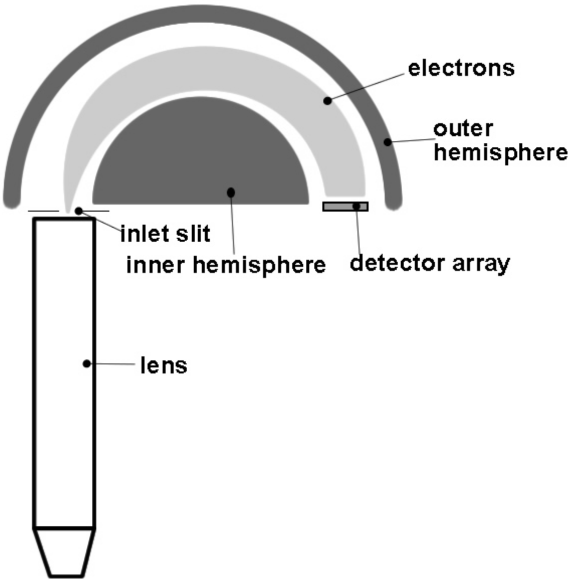

Figure 1.8: Basic hemispherical analyser and lens schematic

### 1.4.1 CHA Operation

The concentric hemispherical analyser, as it's name suggests, is made of two concentric hemispheres, the inner one being convex and the outer concave. The inner hemisphere has a positive potential relative to the retard potential, and the outer hemisphere has a negative potential relative to the retard potential, as shown in figure 1.9 [28]. This gives rise to an electric field proportional to 1/r, which has the effect of accelerating the incoming electrons toward the centre of the analyser, making them follow an elliptical path. The combination of the analyser's geometry and the potential means that only electrons with kinetic energies within a certain range travel around the analyser and emerge from the analyser's exit slit. This range of energies is centred upon a value known as the analyser's pass energy. Electrons with kinetic energy greater than this will fall outside of the exit slit, and electrons with lower kinetic energy will fall closer toward the centre of the analyser than the exit slit.

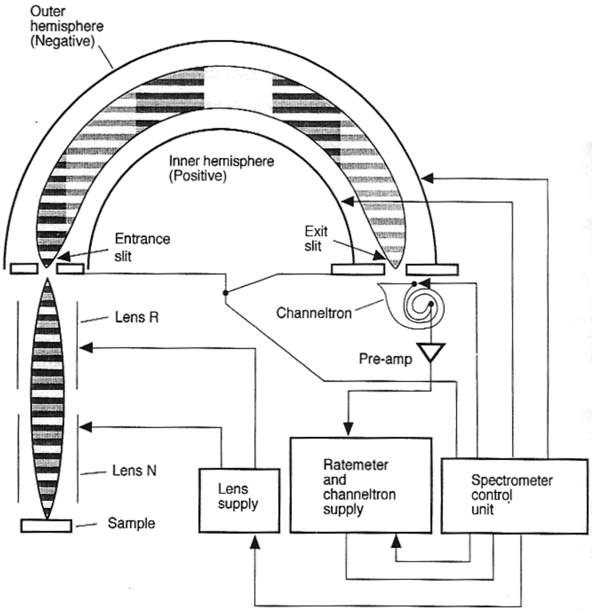

Figure 1.9: CHA and power supply schematic

The entrance slit restricts the radial range at which electrons can enter the analyser. If the entrance slit width is wide, more electrons may enter the analyser, but will do so at a range of positions, reducing the resolution of the analyser. Conversly, using a smaller entrance slit will improve the resolution of the system at the expense of signal level, As the exit slit has a finite size, electrons of a range of energies can escape the analyser. Within this range, electrons with lower energy will exit closer toward the centre of the analyser. Conversely, electrons with higher energy will land towards the outside of the analyser. This dispersion allows position sensitive detectors to image parts of the spectrum. In non-position sensitive detectors, this range of energies represents a loss of resolution. The size of the exit slit is selected to allow the most appropriate trade-off between resolution and count rate.

### 1.4.2 Electrostatic Lens Operation

The electrostatic lens performs two functions - it collects electrons escaping from the surface of the sample and focusses these electrons onto the inlet plane of the analyser. It also retards the kinetic energy of electrons, by varying it's potential relative to the potentials of the analyser hemispheres. By varying the retard potential, the incoming spectrum can be scanned across the exit slit of the analyser, as shown in figure 1.10.

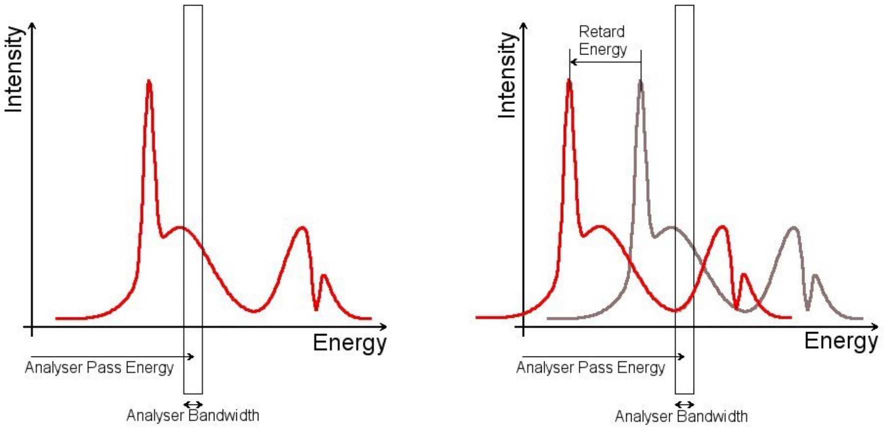

Figure 1.10: Varying the retard potential scans the spectrum

Analysers also have variable entrance and exit slits. . Electrons entering the lens are focused and pass through the entrance slit into the hemispheres.

Electrons of different energies are dispersed at the focal plane, and are detected after passing through the exit slit. The most common method of detection is a channeltron that is placed at the focal plane behind the exit slit. However, multi-element detection at the focal plane is a much more efficient method of getting the energy spectrum and the main focus of this thesis is in the application of a recently-developed array detector to detect photoelectrons with a range of energies in imaging mode.

### 1.4.3 CLAM4 Analyser

The analyser used in all the experiments here is a Thermo VG CLAM4 [28]. This is a 150mm mean radius hemispherical analyser. As standard, it has entrance and exit slits that can be set to 0.5, 1, 2 and 5 mm. However, in this application, the exit slit has been modified in order to expose the entire face of the detector module.

The CLAM4 has two methods for scanning spectra; CAE (Constant Analyser Energy) and CRR (Constant Retard Ratio).

#### CAE

In CAE (Constant Analyser Energy) mode - also known as Fixed Analyser Transmission (FAT) mode, the pass energy of the analyser is held constant as the retard potential is varied. This keeps the resolution of the analyser constant throught the range of the scan. The CLAM4 has a pass energy range of 2eV to 400eV.

**CRR**

In CRR (Constant Retard Ratio) mode, the pass energy of the analyser is varied along with the retard potential. In this case, the ratio of the pass energy to the kinetic energy of the electrons is held constant. This varies the resolution of the analyser as the retard potential is changed. The CLAM4 can set the ratio $E_{pass} : E_{kinetic}$ to a range of values from 1 to 100. At higher kinetic energies, the energy bandwidth the analyser allows through is greater. This mode, whilst prefered for Auger spectroscopy, is less frequently used in XPS applications: In XPS, spectral peaks are generally higher in energy, and the loss in resolution at these higher energies in CRR mode is not acceptable.

## 1.5 Detectors

Once the electrons have been dispersed as a function of their energy, they must be counted. This can be done by using a narrow exit slit and a single channel detector to measure the number of electrons at the analyser's current pass energy once retarded. Alternatively, if a wide exit slit is used, a position-sensitive detector can measure the number of electrons at a number of kinetic energies.

### 1.5.1 Channeltrons

Because the electrons emerging from the analyser constitute too small a signal to be directly detected, this signal must be amplified to detectable amplitudes. This can be done via electron multiplication in a channeltron.

Properly known as a Channel Electrom Multiplier, or CEM, ("Channeltron" is a trade name), is based upon a glass funnel formed into a spiral with an anode at it's end. The anode is held at a positive potential relative to the mouth, whilst the mouth itself follows the retard potential. In order to maintain the same potential difference between the mouth and the anode, the anode potential also varies as the spectrum is scanned. Incident electrons enter the mouth of the funnel, and due to it's shape, hit the wall causing a secondary emission of electrons. Due to the potential difference between the mouth and the anode, these electrons are accelerated further into the funnel. When these collide with the wall, further secondary electrons are released. This process continues down the funnel, meaning a single incident electron can produce an avalanche of around $10^8$ electrons at the anode, enough to easily be detected.

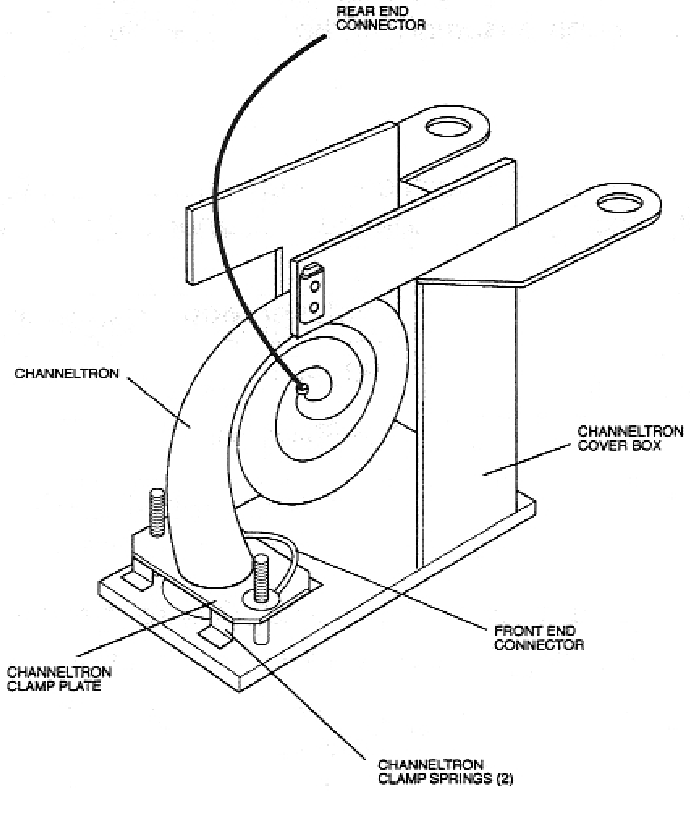

Figure 1.11: A Typical CEM, from [28]

CEMs are well suited to applications where the measured spectrum does not significantly vary within the time taken to scan the spectrum across the exit slit of the analyser. By selecting a narrow exit slit and running the CEM at high gain, high-resolution spectra can be produced.

After each electron avalanche, a CEM requires a finite time before it can produce another of sufficient magnitude to be detected. This has the effect of giving the CEM an upper limit to it's count rate. 2Mhz is considered to be a standard maximum count rate [28].

CEMs also have a finite lifespan - over time, a higher potential difference between anode and mouth is required to maintain the CEM's gain. This must be taken into account when calibrating a system.

Systems have been developed that use a number (typically around 7) of individual channeltrons spread along the dispersive direction of the analyser focal plane, however these are not capable of taking meaningful snapshot spectra, and making channeltrons small enough to fit a suitably large number along the focal plane represents a huge challenge.

### 1.5.2 Imaging Detectors

Whilst a CEM-based system can produce good results when measuring a time-invariant spectrum, the ability to acquire spectra at greater rates is often required. In this situation, an imaging detector - one which can measure at least a significant portion of a spectrum in one go - is needed. There are a range of different detectors that can do this, each with it's own strengths and weakness.

**Micro Channel Plates**

Whilst not a detector itself, a micro channel plate (MCP) is an integral part of many detector systems. Placed immediately before the detector, the MCP is utilised for amplification of the signal, prior to measurement by the detector array. Sensitive not only to electrons, but also ions and photons in the UV to X-ray range, it allows the array module to be used in a wide variety of applications. It consists of a large number of 12 $\mu$m diameter glass-walled channels. A bias, of order 1kV, is applied between the front and rear faces of the MCP, with the result that an incident electron, upon collision with the channel wall, releases a number of secondary electrons that, in turn, go on to collide with the channel walls, producing an avalanche of electrons that emerges from the rear of the MCP (figure 1.12). A single incident electron can produce around $10^7$ electrons exiting from the MCP, allowing this single incident electron to be detected by the array.

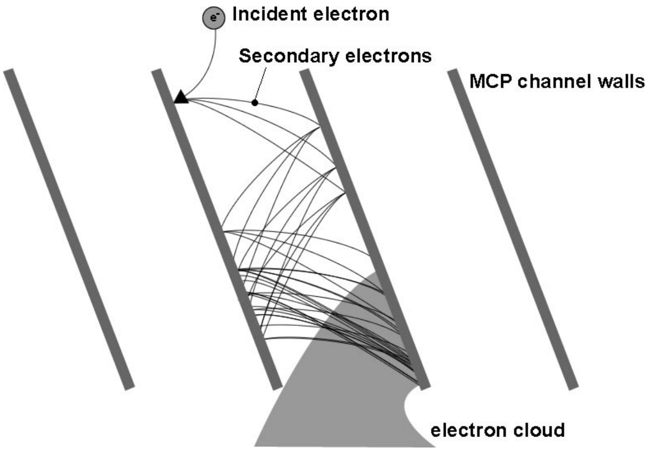

Figure 1.12: Electron avalanche in MCP

### CCD and Phosphor

Detectors have been implemented using a phosphor screen and ccd camera in conjunction with an MCP. Emerging electron clouds from the rear of the MCP impinge upon the phosphor screen, causing it to give off a pulse of light. This light is then detected by a CCD array. This type of detector is commonly used where two dimensional information is needed, but can be prone to noise.

### Delay Line Detectors

A delay line detector consists of a conductive strip, parallel to the dispersive direction of the analyser. An incident cloud of electrons out of the back of the MCP will cause electronic charge to spread outwards from it's impact point. Because this charge front travels at a finite speed, the difference in arrival times at each end gives an indication of the position of impact on the strip. The simplicity of this detector is offset by it's inability to accurately position more than one electron cloud at a single time.

### Counting Detectors

Counting detectors, such as the one developed at Aberystwyth [23] are conceptually the simplest type of imaging detector. They act as an array of independent channeltrons, each with it's own signal processing and counter. These present a greater challenge for accurate calibration but can operate very quickly and with high count rates. These detectors are covered in greater depth later on.

## 1.6 Real-Time XPS

By developing a system that can acquire spectra at a much higher rate ( 1 per second), it becomes possible to observe changes in spectra as they occur. Previously impossible observations become feasible, and experiments that may have taken days can be done in minutes. For a process that takes place over a timespan, the spectrum can be measured at various points in the process, allowing transitionary stages to be observed.

During a deposition experiment in which a substrate material is covered with a compound from an evaporation source such as a knudesn-cell (known as a k-cell), the spectral peaks of the substrate material become attenuated as peaks associated with the deposition material appear and increase in intensity. During this, the spectra will change significantly during the time it takes to scan the spectrum. Therefore, in order to document the process using a single-channel detector, the deposition must be stopped at regular intervals so spectra can be taken. This process is time-consuming, laborious and a potential source of error. With a multichannel detector, spectra can be measured at a rate significantly faster than the changes in the spectra. Other experiments, such as annealing or desorption, which involve heating the sample cannot be suddenly halted in this way. In these cases, multichannel detectors are the only way in which intermediate spectra can be satisfactorily measured. Using a multichannel detector, the changes in peak shape and intensity can be seen.

In single detector systems, being able to increase the spectrum measurement rate to this extent has not been a simple matter of sweeping spectra across a channeltron faster - In order to maintain resolution, the exit slit of the analyser must be narrow. This reduces the electron flux into the collector of the channeltron and necessitates longer collection times to reduce noise. In addition to this, the entire electron optics system can be likened to a complex shaped capacitor - in other words, it has a time constant applicable when changing potentials within it; after any step change in voltage, it will take a finite amount of time for the potentials within the electron optics system to stabilise upon their new values, limiting the speed at which the spectrum can be swept. If the spectrum does not significantly vary within the time taken to scan a spectrum, then snapshots can be taken, but only at a maximum rate of approximately tenths of hz.

Multichannel detectors allow snapshots to be taken at rates high enough to allow desorption, deposition, annealling and so on to be watched. Other techniques become possible as well. Snapshots can be taken at alternating different points in the spectrum throughout an experiment, allowing peaks at widely spaced points in the spectrum to be monitored. Additionally, the wider exit slit allows entire spectra to be swept much faster than in single channel systems. Rapid sweeping enables the entire spectrum to be measured throughout an experiment. This will not give equal time resolution as taking snapshots, but still will be faster than using a single channel system.

# Chapter 2

# System Description

## 2.1 Overview

The REES system currently in operation uses, as it's sensor, an array of 768 independent, electron-sensitive detectors (the detector array) behind a multi channel plate (MCP), together known as the array module [14]. This module is mounted on the focal plane of a CLAM4 electron energy analyser, much like a traditional channeltron. On the inlet of the analyser, as usual, is an electron lens focused upon the sample being investigated. The system has been operated in a variety of settings, including twin-anode and monochromated X-rays here at Aberystwyth, synchrotron light at Beamline 4.1 at Daresbury.

The main advantage of using this multi-channel detector array in place of a channeltron is speed. The detector array allows for a spectrum to be taken in a mere fraction of the time required by a channeltron system. The system can be operated in one of three modes: swept, snapshot and virtual channeltron. Scanned mode can be likened to a standard channeltron, in that the spectrum

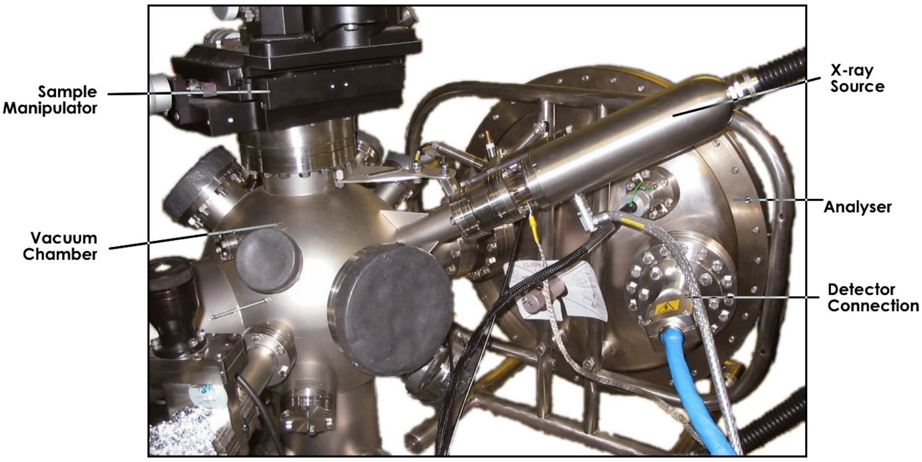

Figure 2.1: REES System

is swept across the array by varying the retarding potential of the analyser. However, as the array consists of, in effect, 768 channeltrons, 768 spectra are produced. If all these spectra were simply summed, this would give an equivalent result to that of a channeltron behind an exit slit of the same size as the array. However, by using a process known as weaving, each spectrum recorded by a single channel is slightly shifted before summing, to allow for each detectors different position on the focal plane of the analyser. This method gives results were the count rate is comparable to that obtained by a channeltron behind a 2cm exit slit, and a resolution approaching that of a channeltron behind a 25 $\mu$m exit slit.

In snapshot mode, the retarding potential remains unchanged, so that the array keeps looking at a single segment of the energy spectrum. The size of this segment is governed by the pass energy of the analyser; higher pass energies give a wider range, low pass energies a smaller range. The segments position on the spectrum is controlled by the analyser's retarding potential. When this segment is placed to coincide with a feature in the spectrum, say a carbon $C1^s$

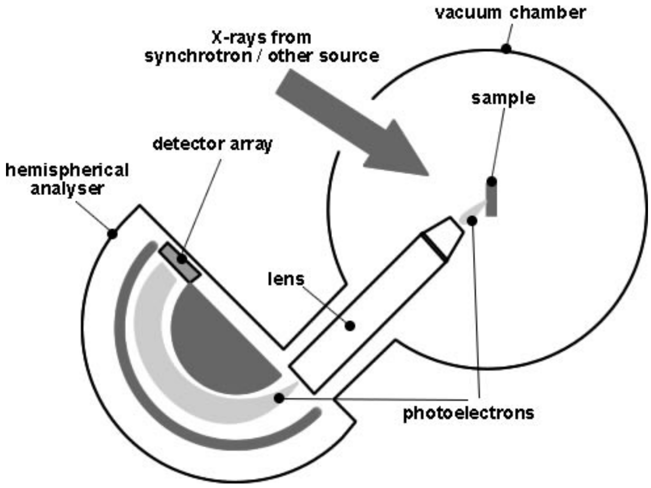

Figure 2.2: REES System schematic

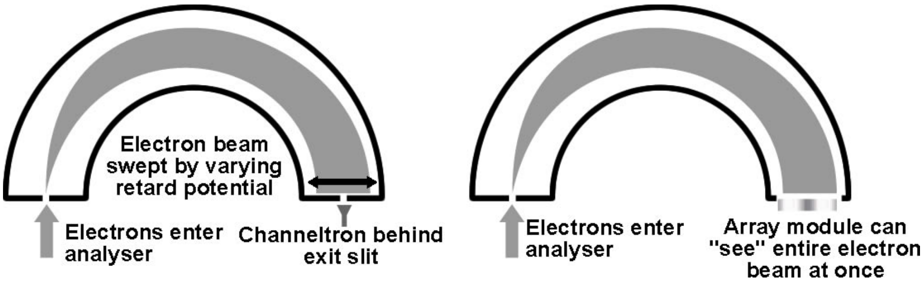

Figure 2.3: Comparison of Channeltron-based (left) and Multichannel detector-based (right) systems

peak, changes to the peaks position, size and shape can be monitored during experiments, such as heating the sample or depositing material on the sample. Although the array can run much faster, spectra are usually taken at a rate of 0.1 to 10 spectra per second, dependent upon the flux of incoming electrons. For a little sacrifice of resolution in the time domain, the system can take snapshots, alternating between two or more points on the spectrum, allowing for several peaks to be monitored during the course of an experiment. The limiting factor here is the time constant of the analyser, which being in effect a large capacitor, takes some time to settle upon a new point in the spectrum when a step function is applied to its voltages. Virtual Channeltron mode uses the summed output from a subset of channels to simulate the behaviour of a channeltron with an analyser exit slit equal to the combined width of the selected channels.

## 2.2 MCP

The MCP is utilised for amplification of the signal, prior to measurement by the detector array. Sensitive not only to electrons, but also ions and photons in the UV to X-ray range, it allows the array module to be used in a wide variety of applications. It consists of a large number of 12 $\mu$m diameter glass-walled channels. A bias, of order 1kV, is applied between the front and rear faces of the MCP, with the result that an incident electron, upon collision with the channel wall, releases a number of secondary electrons that, in turn, go on to collide with the channel walls, producing an avalanche of electrons that emerges from the rear of the MCP. A single incident electron can produce around $10^7$ electrons exiting from the MCP, allowing this single incident electron to be detected by the array.

In this application, a stack of two MCPs is used, with the MCPs arranged in a chevron formation to maximise the number of electron-wall collisions at the entrance of the second MCP. The use of two MCPs has two advantages over using a single MCP: The first is that a greater gain and sensitivity is obtained compared to using just one MCP. The second advantage is that the output pulse size distribution is modified (figure 4). The resulting distribution makes the placement of a threshold level above which pulses trigger the counters less

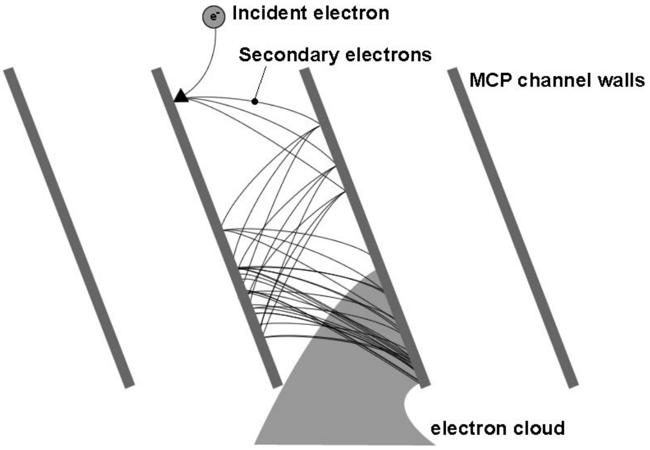

Figure 2.4: Electron avalanche in MCP

critical.

The disadvantage of using two MCP plates is that a pulse of electrons emerging from the first MCP will spread whilst traversing the space between the two MCPs, broadening the apparent size of any features in the spectrum. This broadening also occurs in the space between the rear face of the MCP stack and the detector array. This effect has profound implications for the resolution and uniformity of the array module and will be discussed in full later.

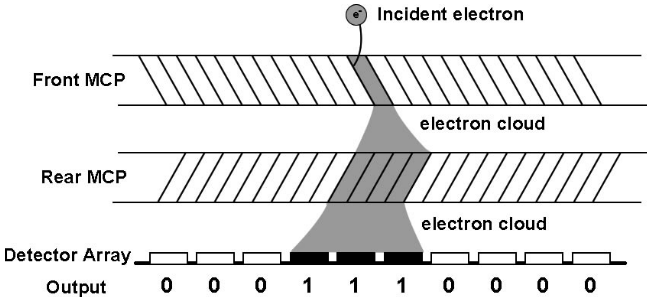

Figure 2.5: Pulse spreading causes a single event to trigger numerous channels

## 2.3 Detector Array

Although originally developed for use in mass spectroscopy [13], the current iteration of the detector array is being utilised for electron energy spectroscopy [14]. Due to the versatility of the MCP, this change of purpose has not required modification of the array, although changes have been made over time as improvements to the design have become possible as silicon chip technology has progressed.

The array itself is based upon a single custom ASIC (Application Specific IC) mounted on a ceramic wafer. On top of the chip is an array of metal anodes measuring 3mm in the non-dispersive direction and 17$\mu$m in the dispersive direction, spaced on a pitch of 25$\mu$m. For the majority of the work presented here, the array consisted of 768 of these detectors, giving the array itself a length of 19.2mm. Also on the chip is electronics to operate the detectors and collect data, consisting of amplifiers, counters and digital circuitry to collect data from each channel sequentially and send it to the control unit. The amplifiers respond to a group of electrons emerging from the rear of the MCP by outputting a digital signal, which is passed onto that channels corresponding counter. Currently, the counters are 16-bit devices, allowing up to 65534 events to be counted in any one cycle of operation before saturation occurs. The maximum value countable by a 16-bit device, 65535, is reserved to prevent the counters overflowing and returning spuriously low counts.

Due to the digital nature of the system, the dark count rate from the detector array itself is negligible compared to that of the MCP, as discussed in 3.2.3.

The ceramic wafer sits in an aluminium cup, with electrical connections made by a bed of nails: spring-loaded pins against gold contact points on the underside of the wafer. On top of the wafer are mounted the two MCPs, held in place by stainless steel springs. Above the MCP's is a molybdenum plate with an aperture corresponding to the position and size of the MCPs. This plate is secured to the aluminium cup, holding the MCPs and detector array securely in place. A fine wire mesh can be placed between the MCPs and cover plate to minimise the distortion in the analysers internal electric field caused by the hole in the plate.

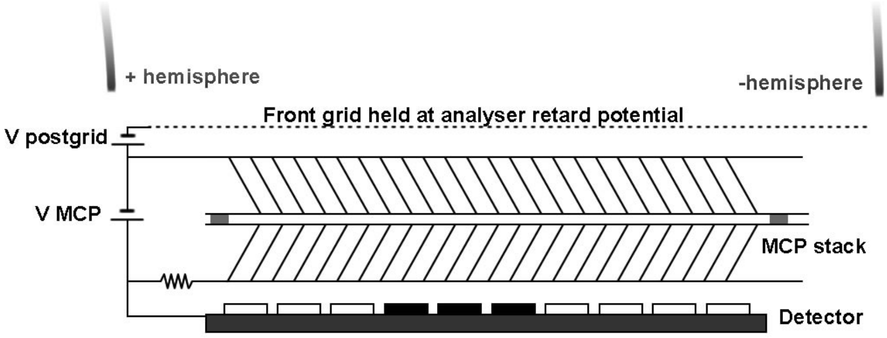

Figure 2.6: Potentials at detector array

The postgrid voltage, the bias between the front face of the MCP and analyser potential, can be set as desired. This has the effect of limiting the number of stray low energy electrons entering the MCP [7]. Because the grid follows the analyser's retard potential, and the potentials of the MCP faces and detector are relative to this, the potentials of the whole system must follow the retard potential. Therefore it is necessary for the detector and it's control system's potentials to "float" in oder to be able to follow the retard potential. This is made possible by the control's floating power suuplly and fibre optic data link.

The entire module is placed on the focal plane of the electron energy analyser, at vacuum, and a multi-pin feedthrough connects it to the outside world.

Figure 2.7: Detector array on ceramic substrate

## 2.4 Control Unit

The control unit, developed specifically for this application by Daresbury and RAL, is connected to the array module via a multi-pin feedthough and to a standard PC via Ethernet. The connection to the array module carries voltages for the MCP and postgrid, as well as control to and data from the detector array itself. A floating power is used to supply to isolate the controller from the mains power supply and the Ethernet connection utilises a fibre-optic link to ensure the network is electrically isolated from the potentially damaging voltages within the controller. A standard PC is used to interface with the control unit, to set the array operation parameters and to collect the data from the array. This PC is also used to control other elements of the REES system, such as sample heaters and K-cells. In addition to this, the PC also can collect data from other sources, for example thermocouples for monitoring sample temperature. TCP/IP is used for communication over the internet between the PC and the control unit.

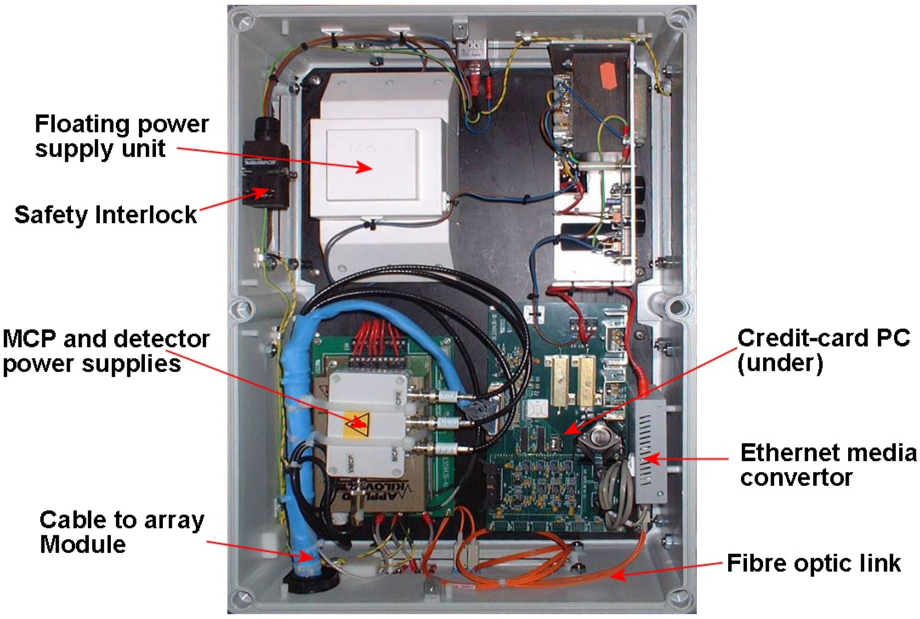

Figure 2.8: Schematic of control unit

## 2.5 Electron Optics

In electron energy spectroscopy, the electrons given off from the sample are collected by an electron lens and dispersed by an electron energy analyser. In this case, the lens used is a VG LN04 and the analyser a VG CLAM4, a hemispherical electron energy analyser [28]. The CLAM4 is a 150mm mean radius, 165deg true hemispherical analyser. As standard it comes with selectable 0.5mm, 1mm, 2mm and 5mm entrance and exit slits, although the outlet slit is removed in this application to allow the entire focal plane to be imaged by the detector module. The remaining inlet slit can be used to control the incoming flux of electrons, although increased flux is at the expense of poorer resolution.

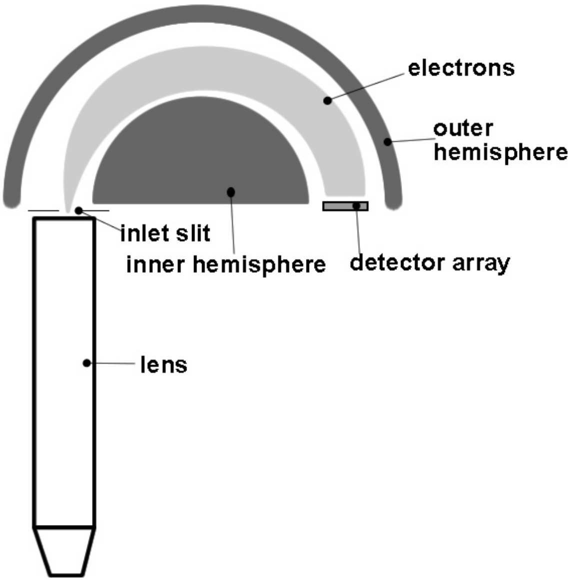

Figure 2.9: Electron lens and analyser

The installation of the array module has allows the focal plane of this analyser/lens combination to be imaged, revealing distortions of spectra as measured by this analyser/lens combination. When using a single channeltron, these aberrations are of little consequence, as it is merely the total number of electrons that is recorded at any one time, rather than their energy distribution. However, due to the nature of the array module, these aberrations must be quantified and corrected in order to obtain accurate spectra. This was done with a combination of modeling and experimental techniques and is discussed in full later.

## 2.6 Applications

### 2.6.1 X-ray Photoelectron Spectroscopy

The system here described has been used extensively for X-ray Photoelectron Spectroscopy both at Aberystwyth and beamline 4.1 at Daresbury. Used for surface analysis, in XPS a sample under study is illuminated with X-rays, ejecting core level electrons, the energy distribution of which is measured using an electron energy spectrometer. This gives information about the binding energy of electrons within the sample. Developed in the 1960s, XPS has been heavily used in many research applications. With the addition of a detector capable of taking spectra within seconds rather than tens of minutes, real-time XPS becomes possible.

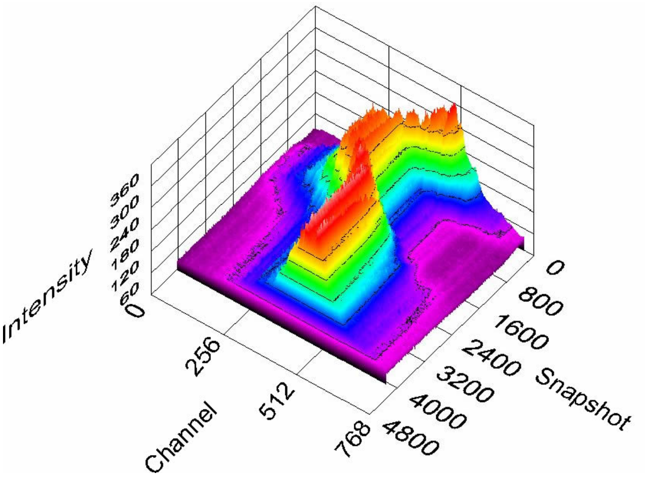

Figure 2.10: Example real-time XPS spectrum

In real-time XPS, the array is operated in snapshot mode, looking at one or several features in the spectrum whilst, for example, the sample has material deposited upon it. This allows for the observation of effects such as energy peaks from the base material becoming less intense as more material is deposited. Prior to this detector array, this had to be done in stages: depositing a small amount of material, then taking a spectrum before depositing more material and so on, a process that could take hours. Other phenomena that were previously difficult or impossible to observe can now be watched easily, for instance, the clustering process undergone by freshly deposited SnPC on a Gallium Arsenide substrate. The system has also been used to watch in real time carbon 1s peaks in diamond become more intense as the diamond is annealed.

### 2.6.2 Other Applications

As the MCP is sensitive to not only to electrons, but also ions and high-energy photons, the array module can be used, with little or no modification for any application where a one-dimensional position sensitive particle detector is needed, for example mass spectrometry, photon spectroscopy, transmission electron energy loss spectroscopy to name but a very few. At the time of writing, it is hoped to further develop the detector array into a two-dimensional device which will find applications in an equally wide range, including, but not limited to, crystal diffraction techniques, such as X-ray diffraction and LEED (low energy electron diffraction), astronomical imaging and the like.

# Chapter 3

# Aberrations

In this section, aberrations arising from the array module are introduced, analysed and measured where possible, leading to the development of an algorithm to correct for these distortions.

## 3.1 Electron Optics Aberrations

The electron energy analyser itself introduces aberrations into the spectrum measured at the focal plane of the analyser. In order to correct these, they must first be understood. To achieve two simulations of the analyser were developed - one using MathCAD, and one using the SimION package.

### 3.1.1 Analytic Simulation - MathCAD

**Derivation**

This simulator models an ideal analyser. To this end, certain assumptions have been made, in order to simplify the modeling. These assumptions are:

- The analyser is completely evacuated - there is no gas inside that may affect the electrons' trajectories.

- The analyser contains a perfect central force field - it behaves as if a single point charge were at the centre of the analyser. This ignores distortions in the electric field towards the ends of the analyser, but reduces the complexity of the simulation.

- The space charge effect - mutual repulsion of a group of electrons - is ignored as in the system used, this effect is negligable [29].

As the system is modelled as a central point charge, electrons within the analyser follow closed elliptical paths analogous to Keplerian planetary motion with one focus of the ellipse coincident with the centre of the analyser.

Given the semi major axis of the ellipse which can easily be found from the energy of the electron, and the fact that a ray of light from one focus of an ellipse will reflect off the perimeter of the ellipse and pass through the other focus, and this path will be of length 2a where a is the semi major axis, the equation of motion for the electron can be found.

Assuming a 1/r potential [30], electrons travel in ellipses, with the centre of the analyser at one focus. The electrons in this case when within the analyser have the equation of motion:

$$\ddot{\mathbf{r}} + \frac{qk}{m}\frac{\mathbf{r}}{r^3} = 0 \tag{3.1}$$

Solving this and simplifying gives the analyser function:

$$r_{out} = r_{in}^2 E_k \frac{1 + cos(2\theta)}{2E_{pass}(R_1 + R_2) - E_k r_{in}(1 + cos(2\theta))} \tag{3.2}$$

Where:

- $r_{out}$ is the exit radius of an electron
- $r_{in}$ is the entrance radius of an electron
- $E_k$ is the kinetic energy of an electron
- $\theta$ is the entrance angle of an electron
- $R_1$ and $R_2$ are the inner and outer radii of the analyser hemispheres
- $E_{pass}$ is the analyser's pass energy

**Use of Simulator**

The simulation is run a number of times, with the electron starting positions, angles and energies chosen from suitable distributions and the exit position calculated from each run, building up a distribution of exit positions.

The simulator can be operated in two ways, corresponding to using a channeltron or a detector array. When in channeltron mode, the simulator simply counts how many electrons land within the exit slit of the analyser. In array mode, the simulator returns a histogram of number of electrons landing on the detectors in the array. The number, pitch and position of the detectors can be configured, as can the position, size and shape of the entrance and exit slits.

The simulator allows batches of electrons to be run through the analyser. These batches can be given distributions of energy, entrance angle and position within the entrance slit. This is much more useful than simulating single trajectories as it returns a distribution of exit positions. The energy distribution put in corresponds to the energy spectrum being measured. In an ideal world, the entrance angle and position of the electrons would not be distributions, but single values, so that electrons with a particular energy only land at one point at the other end of the analyser. However, as entrance position and angle have distributions, so does the exit point for a single energy value. This simulator allows these exit distributions to be found.

One result was that any angular deviation from zero degrees (tangential to focus) of the electron leads to the electron falling inside of where it would had it entered tangentially, regardless of which way the angular deviation is. Distributions in energy position have a more intuitive effect, where a broadening in the exit position causes a symmetric broadening in the exit position distribution.

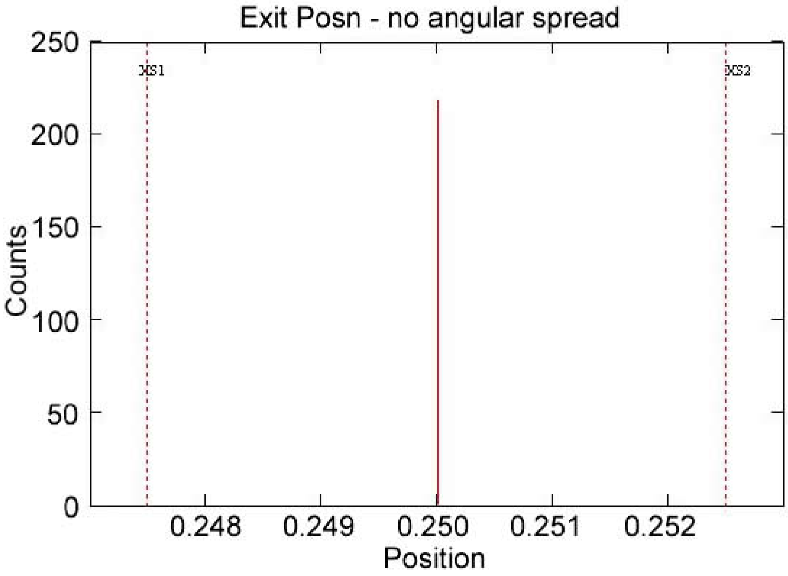

Figure 3.1: Electron distribution at analyser focal plane with no angular spread at input

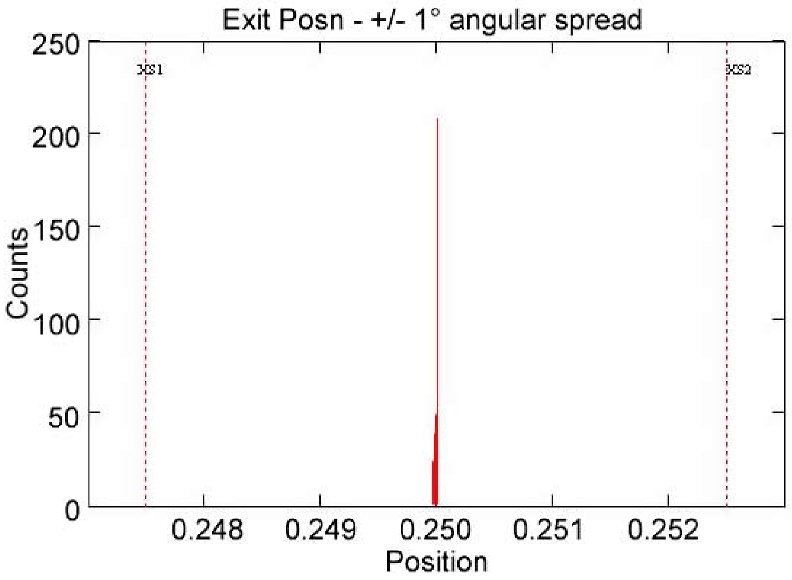

Figure 3.2: Electron distribution at analyser focal plane with 1 deg angular spread at input

From these it can be seen that broadening the angular spread of electrons as they enter the analyser broadens the exit position distribution, but only towards the centre of the analyser. This means that broadening the angular distribution will not only broaden features in the spectrum, but also introduce an asymmetric distortion.

### 3.1.2 Physical Simulation - SIMION

The analytic simulator previously discussed models the behaviour of electrons in an ideal analyser. Whilst useful as a first-order approximation, it does not take into account any effects caused by limitations of the CLAM4 analyser in reality. In order to model effects such as field distortions towards the ends of the analyser, the ion optics simulation package SIMION[10] was used. A simple

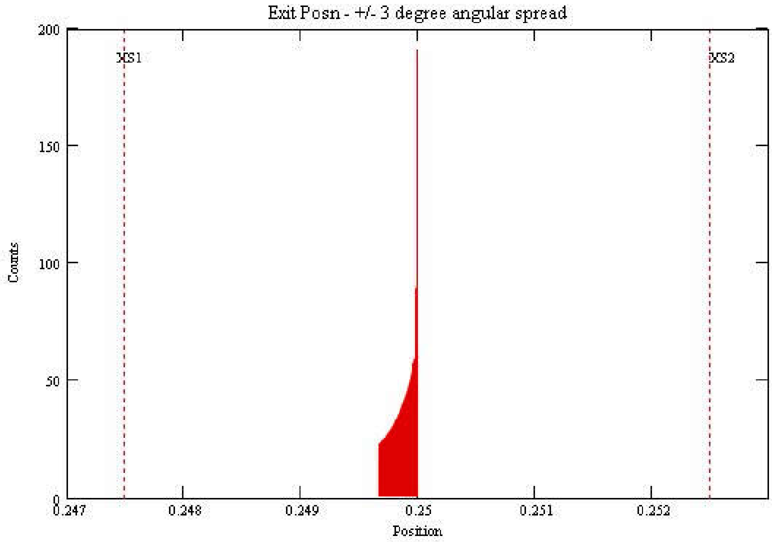

Figure 3.3: Electron distribution at analyser focal plane with 3 deg angular spread at input

model of a hemispherical analyser was created in SIMION and electrons were then "flown" through the model analyser so that their behaviour under certain conditions could be observed.

### Electron Trajectories

Using the model built in SIMION, groups of electrons were simulated within the analyser, and given a range of energies and entrance angles. The simulator showed the exit positions of the electrons, shown in figures 3.5 - 3.8. In each of these figures, the analyser's entrance slit is on the left, and it's exit slit on the right.

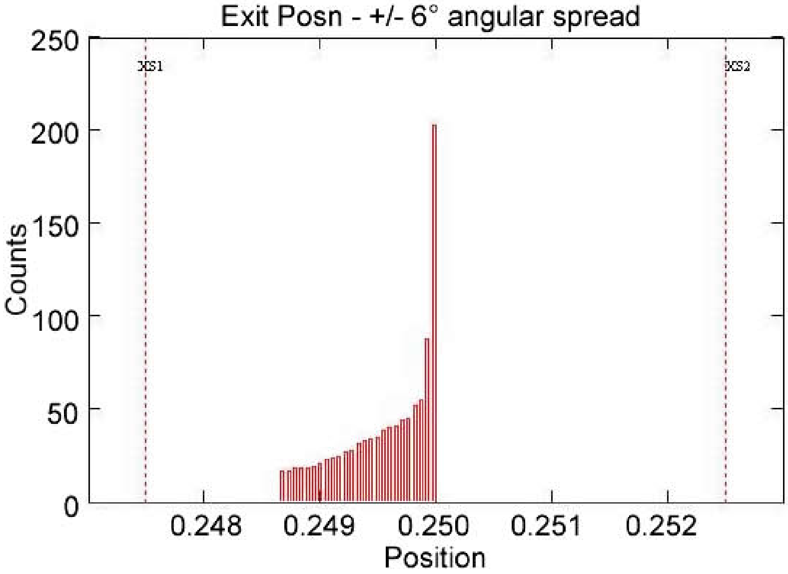

Figure 3.4: Electron distribution at analyser focal plane with 6 deg angular spread at input

Here, a group of electrons with KEs between 1.63 KeV and 1.91 KeV enter the analyser. As expected, and as shown previously, the electron's exit positions are dispersed, with higher energy electrons emerging at a greater radius.

Here, a group of electrons enter the analyser at a range of angles (± 15deg). Non-tangential electrons emerge at lesser radii than the electron entering at 0deg, (highlighted)

To compare the effects of angular distribution and energy distribution, three groups of electron where flown through the simulated analyser. Each group consisted of three electrons with kinetic energies varying from 1.73KeV to 1.83KeV, and the groups are given entrance angles of -3deg, 0deg and 3deg.

A closer view of the electrons at the exit of the analyser shows that for any given KE, tangential electrons exit at greater radii than non-tangential electrons.

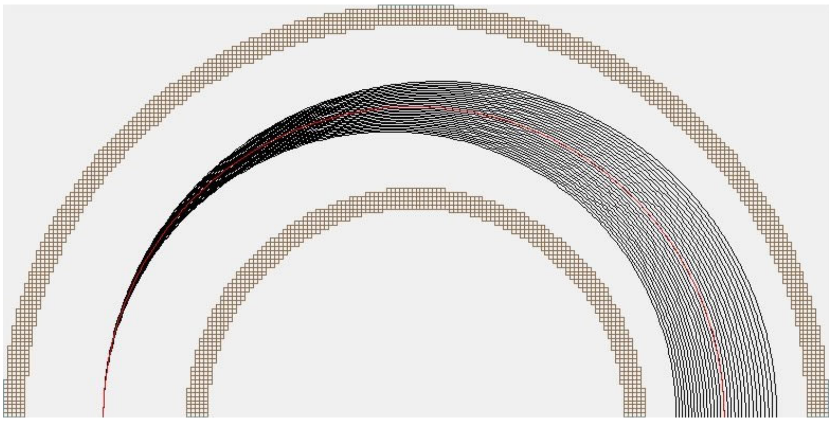

Figure 3.5: Effect of KE distribution

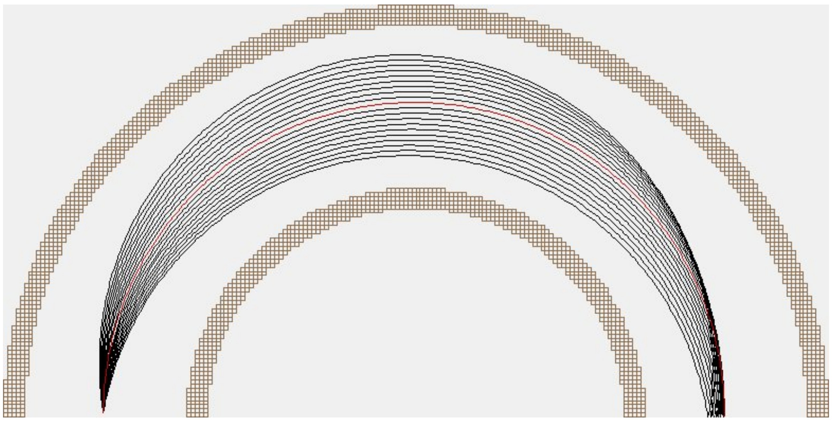

Figure 3.6: Effect of angular distribution

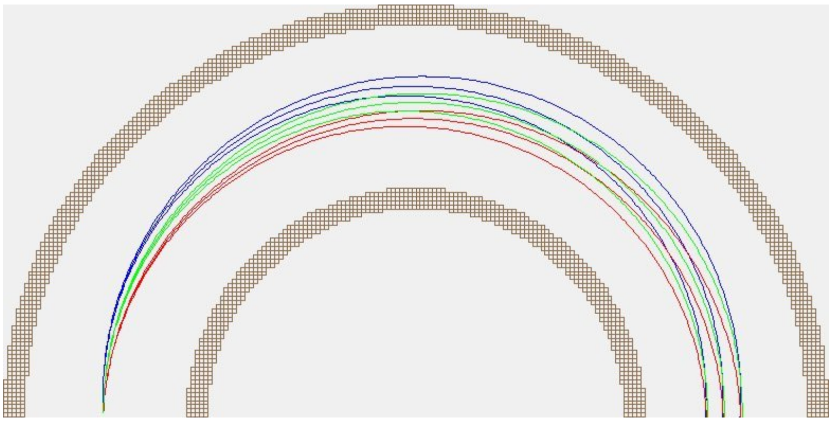

Figure 3.7: Effect of angular and KE distribution

**Field Lines**

SIMION can also be used to show electric potential lines within a system, such as the analyser. Here, the end of the analyser is shown, with the potential lines displayed. The distortion near the exit plane can be seen in figure 3.9.

The distortion in the potentials shown here will in turn distort the measured spectrum.

## 3.2 MCP

The first element of the array module encountered by electrons passing through the analyser exit slit is the first of the two MCP plates. The MCP provides the primary amplification in the detector system and dominates many of the overall characteristics of the system.

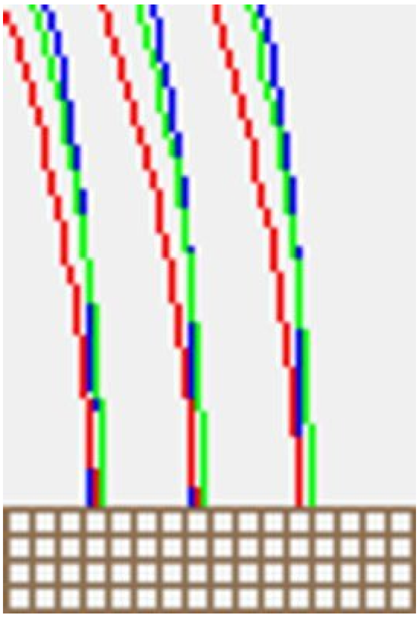

Figure 3.8: Effect of angular and KE distribution - detail view

### 3.2.1 Non-Uniformities

In the manufacture of components, such as MCP's, it is inevitable that various tolerances have a finite value. In the case of the MCP, this manifests itself as a channel-to-channel variation in both gain and sensitivity, resulting in an output varying on a per-channel basis when given a uniform input. [24]

### 3.2.2 Non-Linearities

Because the output of an MCP must be finite, there must exist an upper limit upon the input, above which increasing the input will not lead to a corresponding increase in the output. This is known as saturation and occurs because of the finite time it takes for the MCP channels to recharge after an electron avalanche: when the rate of incident electrons becomes too high, there is a lack of electrons with the walls of the channel to sustain a cascade of secondary

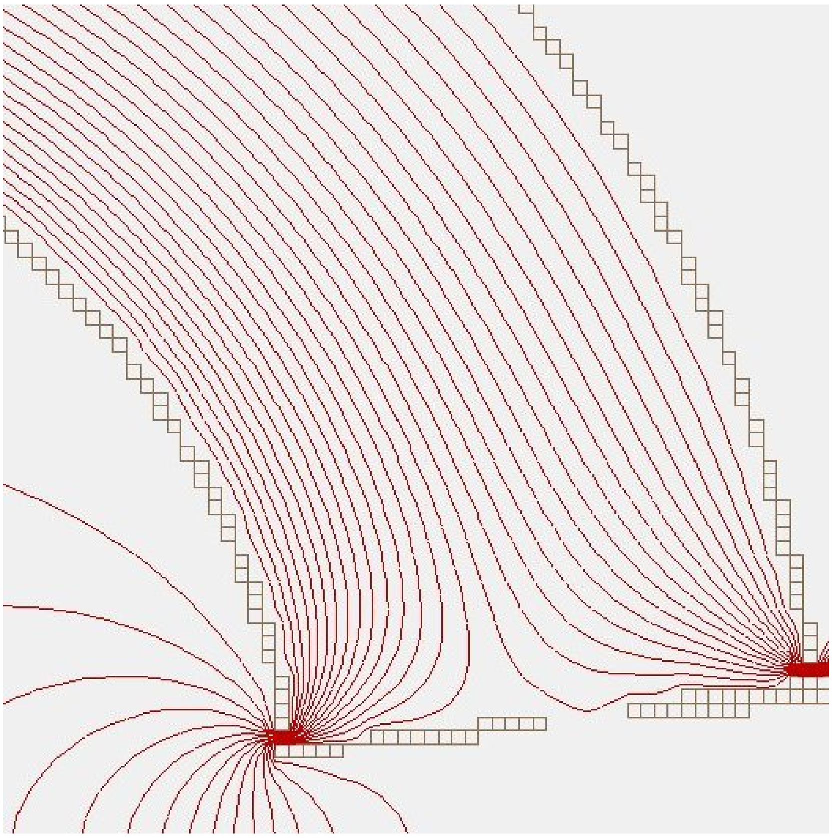

Figure 3.9: Electric fieldlines at end of hemispherical analyser

electrons [2],[17],[19].

Between the dark current limit (See 3.2.3) and the saturation limit, an ideal regime would be a direct linear relationship between input and output and for part of the input range, this is approximately true. However, the most noticeable departure from this behaviour is shown as the input increases toward saturation point, the output also approaches it's saturation value but in an asymptotic-like fashion as seen in fig 3.10.

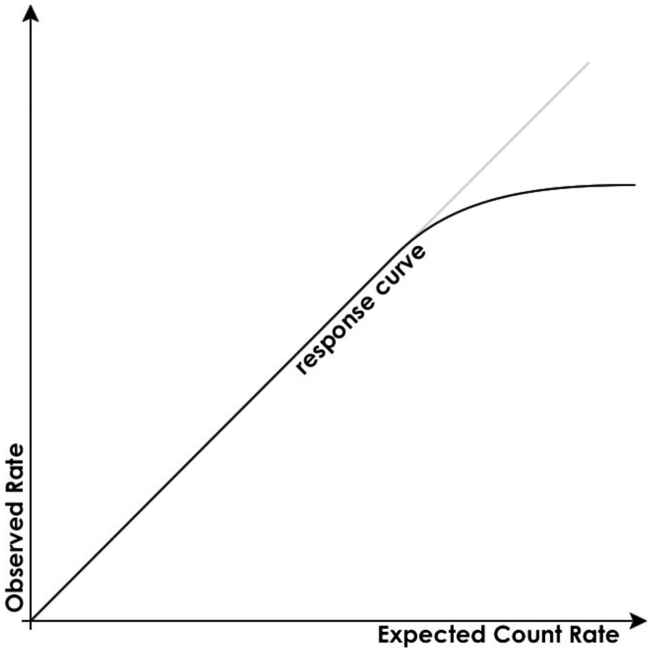

Figure 3.10: As the MCP nears saturation, it's gain falls off

### 3.2.3 Dark Count

The glass from which the MCP is constructed contains potassium, which is a beta emitter. The electrons it gives off are capable of triggering an electron avalanche within a channel of the MCP, and hence generating a count on the readout device [18]. This effect, the *dark current*, places a lower limit on the input of the system: below a certain threshold, the dark current rate will be significant compared to the real signal and give a spurious result. The dark count of the MCP places a lower limit on the dynamic range of the system. The dark count rate can be measured by leaving the system running with the X-ray source turned off. This was found [9] to be of order $10^{-4}$ counts per second per pixel, which is not significantly when compared to typical count rates when taking spectra.

### 3.2.4 Lifespan

The performance of an MCP plate will gradually degrade with usage. The amount by which the output of a plate is reduced is a function of total electron flux through it. Given that the second MCP plate in the stack is generally driven to saturation, this plate will degrade at a higher rate than the first stack. This would be, at best, undesirable if the system was being used in an applied setting. However, for the purposes of system characterisation, this may represent an opportunity to obtain data on the differing workings of the two MCPs.

## 3.3 Pulse Spreading

A cloud of electrons in free space will have a tendency to dissipate, due to the effect of Coulomb repulsion: the electrons, all being of equal, negative charge repel each other. Whilst in the confines of a single channel of the MCP, an electron cloud cannot expand laterally, due to the confining walls of the channel. (Longitudinal expansion is possible, reducing the time resolution *** ) However, once the electron cloud emerges from the back of the MCP, the electron cloud is free to expand. At this point, it is also affected by any electric fields present, as well as any divergence borne of the individual electrons ballistic properties. This combination of effects have been variously measured and modeled [P10, P18, P13] and found to depend upon the MCP operating voltage, the voltage and distance between the rear of the MCP and the face of either the subsequent MCPs or the readout device. [In the case of the detector array studied here, the MCP operating voltage is the only routinely varied variable.] This pulse spreading is pertinent to two locations in the detector array: between the two MCPs, and between the second MCP and the readout device. In both instances, the spatial spreading leads to a loss in energy resolution of the measured spectrum: a single event, after its associated electron cloud has been spread out, triggers a number of channels in the array. The effect of this phenomenon is to reduce the available resolution of the device: A single event will trigger a number of channels (Figure 3.11), and conversely, a single channel is sensitive to events occurring in a region wider than the channel itself. (Figure 3.12)

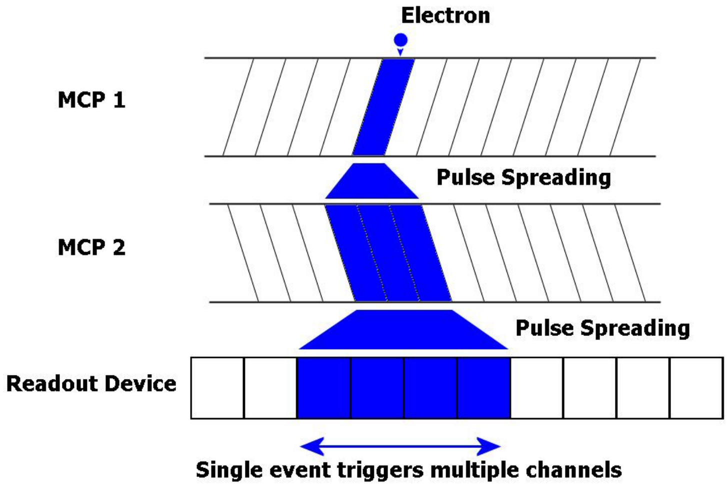

Figure 3.11: Pulse spreading causes a single event to trigger numerous channels

### 3.3.1 Modelling

Vibrans [16] and Tremsin and Siegmund [3] took the approach of modeling the ballistic flight of electrons emerging from the MCP with an additional term representing the Coulomb repulsion experienced by the electrons.

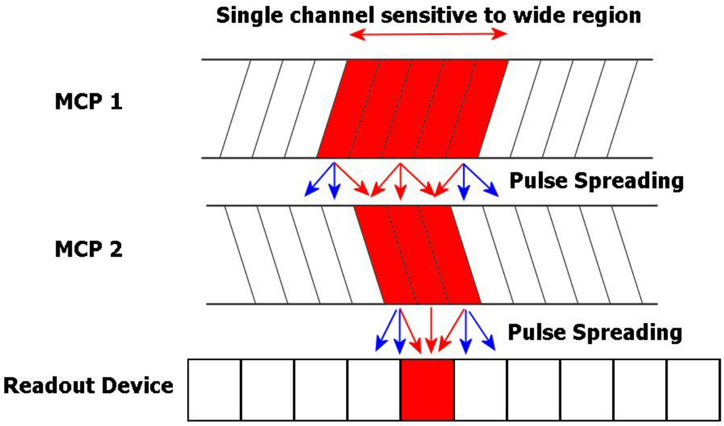

Figure 3.12: Pulse spreading causes a single channel to be sensitive to a large area.

### 3.3.2 Measurement

The extent to which a unique incident electron triggers several channels has not, so far, been measured directly for this device - to do so would require a collimated electron beam narrower than a single channel of the readout device, and the facility to do this has not been present in any of the array's installations. However, the degree of pulse spreading can be inferred from speckling data. By selecting a suitable combination of low incident electron flux, and fast integration times, spectra can be acquired with typically one event each. These events manifest themselves as a string of '1's on an otherwise empty spectrum. Thus, the length of the string of '1's corresponds to the size of the emergent electron cloud, as measured by the readout device. The position of the initial event is not immediately given, but can be taken to be the centroid position of the measured event. [5]

When sufficient data is collected, the frequency distribution of pulse sizes can be calculated, allowing both a mean pulse size to be found as well as a mean pulse shape, obtained by superimposing rectangular functions, whose size and number are given by the pulse size frequency distribution. Alternatively, the mean pulse shape can be approximated as a gaussian.

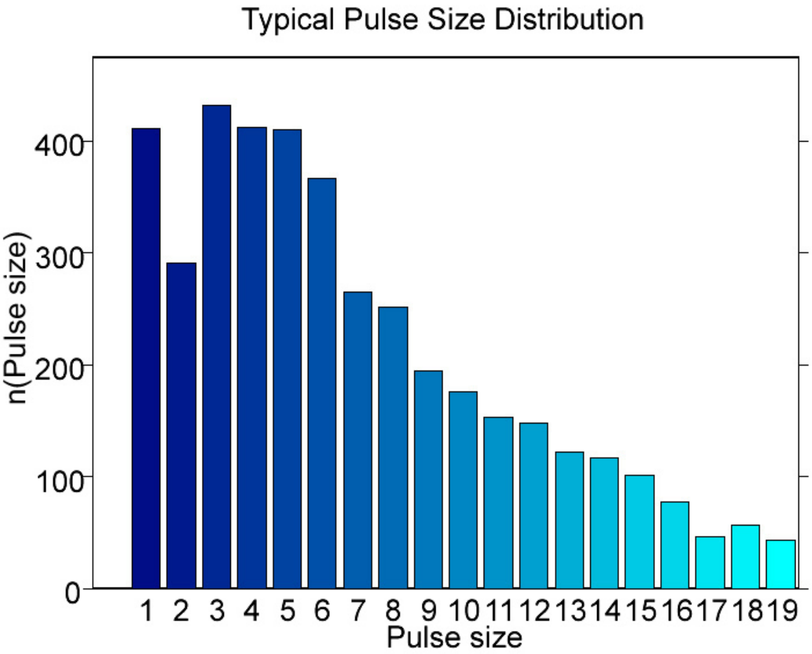

Figure 3.13: Pulse Size Distribution for Entire Array

To generate the mean pulse profile, a number of rectangular functions are summed. The size and height of the rectangular functions is given by the size and number of pulses measured by speckling, as shown in figure 3.14.

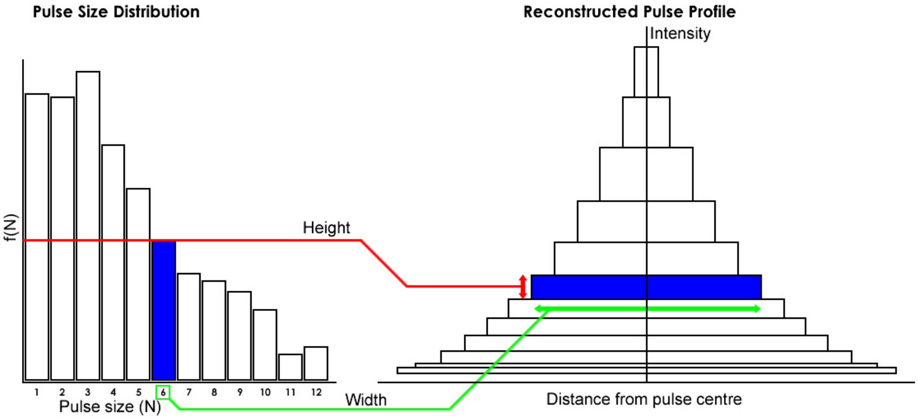

Figure 3.14: Reconstruction of mean pulse profile from speckling data

### Mean Pulse Size

This data on pulse size, necessary for non-uniformity correction can also reveal other information: any variation in the distance between the rear of the MCPs and the readout device across the array will manifest itself as variation in the pulse size distribution across the array - a greater distance will lead to a greater pulse size. By splitting the array into sections and finding the mean pulse shape for each section, rather than for the array as a whole, the straightness and parallelness of the MCP and readout device can be assessed. Variation in mean pulse size across the array has implications for any correction algorithms that attempt to correct for pulse spreading: Whilst using the overall mean (or mode) pulse size to correct the entire spectrum may make a good first order approximation, a more accurrate correction would use an appropriate pulse size for any given section of the array.

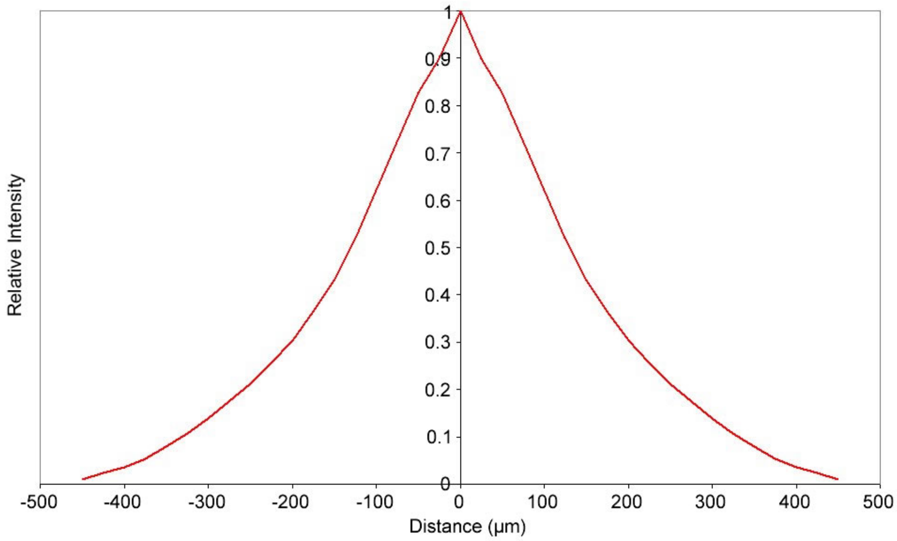

Figure 3.15: Mean pulse profile reconstructed from speckling data

**Mean Pulse Shape**

Once the mean pulse shape has been estimated as shown in figure 3.15, this information can then be used to correct for pulse spreading, as described in section 4.1.4

## 3.4 Readout Device

### 3.4.1 Non-Uniformities

In the same way that manufacturing tolerances in the MCP leads to channel-to-channel variations in performance, the same also holds true for the readout device. Variations in the linewidth of the collection anodes and the thickness of the dielectric layers underneath them will give rise to a distribution of capacitances at the inputs of the sense amplifiers. The matching of the components within the sense amplifiers themselves will be subject to lithographic and other

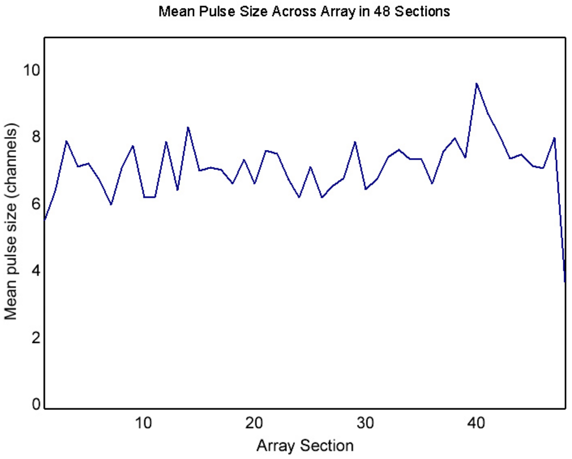

Figure 3.16: Mean pulse profile reconstructed from speckling data

process variations leading to a distribution in the switching thresholds of the individual pixels in the readout device.

## 3.5 Combined Aberrations

Were experimental data available on the aberrations introduced by each individual component of the detector array, it would be a relatively trivial matter to correct for each components contribution to the total distortion. The process, in reverse order, would consist of: correcting for the readout devices distortion; the pulse spreading occurring in the interstitial gap between the second MCP and the readout device; the aberrations from the second MCP plate; the pulse spreading between the first and second plates; finally making corrections for the first MCP plate. However, this information is not available - all we have to go on here is the performance of the module as a whole. It has to be assumed that any correction utilising this available data will give a result that is not significantly dissimilar to sequentially correcting for each component. A further concern is that artifacts may arise in the system due to an interaction between two components. A prime example of such an effect would be moire patterns, outlined below, which arise due to an interference between two regular periodic structures such as the two MCPs. This effect does not arise from either of the two plates, but from the two interacting. These artifacts would not be intrinsic to any individual element of the system, therefore, correcting for each component in turn may actually not produce as accurate a spectrum as correcting for the module as a whole, provided that this is done correctly.

### 3.5.1 Moiré

A feature of geometric optics is that two overlapping similar meshes will produce a periodic interference pattern. This moire effect is also applicable to electron optical systems, such as the MCPs present in the array module. However, this is held to be of little significance unless the two MCPs are in direct contact [4], due to the pulse spreading between the two MCPs, effectively blurring the image of the rear of the first MCP plate.

### 3.5.2 PSF Convolutions

Ignoring, for a moment, the non-uniformity of the MCPs and imagining the gain of the second MCP to be equal to unity, the overall pulse spread function (PSF) of the array module can be thought of as a convolution of the first PSF, between the first and second MCPs and the second PSF, between the second MCP and the readout device. Now, given that the pulse profile emerging from an MCP is generally considered to be a Gaussian [12], the overall PSF would also be a Gaussian: The convolution of two Gaussians of width parameters a and b is a third Gaussian, whose width parameter is given by $\sqrt{a^2 + b^2}$.

The overall pulse spreading, as a function of the spreading between the two MCPs and of the spreading between the second MCP and the readout device has been considered here to be not easily split into it's two components given the data from speckling.

# Chapter 4

# Correction Algorithm

## 4.1 Correction Schemes

A number of strategies for removing distortion originating from the system have been developed and implemented. They are summarised here, before being compared with each other.

### Symbols Used

In discussing the corrections applied, the following symbols are used:

- CS - corrected spectrum
- MS - measured spectrum
- NFF - normalised flat field
- ES - event size
- df - decimation factor
- PSF - pulse spread function

### 4.1.1 Vector Correction

The simplest strategy for correction is to divide a measured spectrum by the relative sensitivities of each channel of the array. This will compensate for non-uniformity originating both from the detector and fom the MCP stack. This can be summarised by equation 4.1

$$CS_i = \frac{MS_i}{NFF_i} \tag{4.1}$$

To obtain the necessary data for this, a section of a spectrum is selected for being as flat as possible; this section is then swept across the entire array, so that each channel of the array has been subject to the same total number of counts. The counts recorded by each channel are then summed to give the total number of events counted for each channel. It is then merely a trivial matter of normalising this data to a mean value of one to obtain the relative sensitivities of each channel.

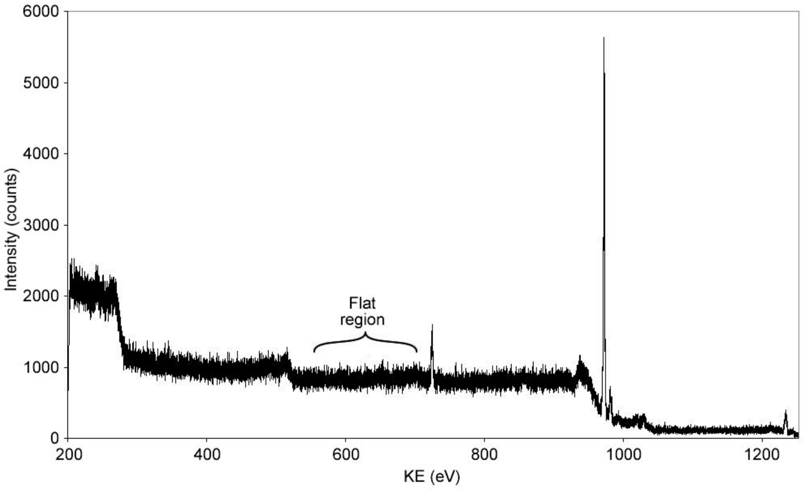

Figure 4.1: Example flat region scan

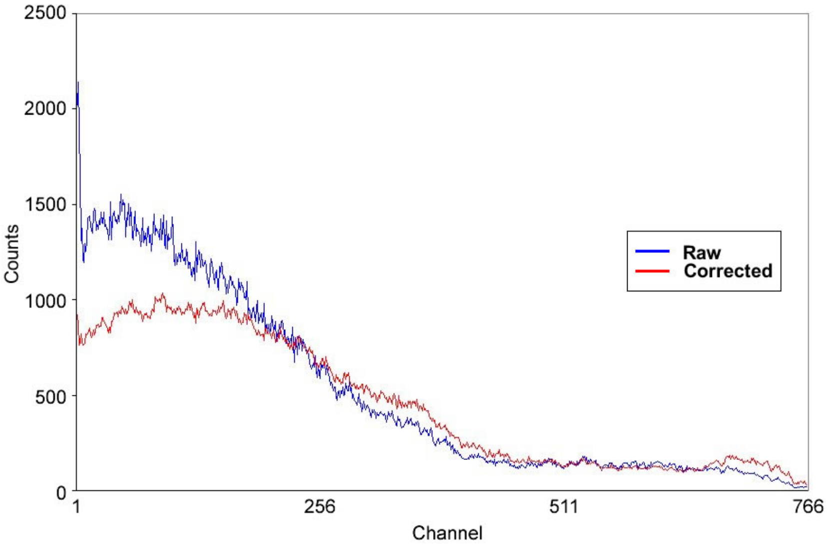

Figure 4.2: Vector corrected data

Whilst this correction is simple and fast to perform, it does not take into account any pulse spreading, any aberrations in the peak shape or any errors due to non-linearity of the array. It is however, useful as an individual stage in a more complete correction scheme, or as an in-flight correction for monitoring real-time experiments.

It can be seen from figure 4.3 that the requisite correction vector changes as the pass energy of the analyser is varied, and also as the MCP voltage is varied (figure 4.4). Changing the pass energy alters the extent to which spectral features are broadened assymetrically. This assymetry causes an increase towards one end of the detector. Increasing the MCP voltage increases the gain of the MCP, driving it towards saturation. As this occurs, the balance of the overall non-uniformity changes between the MCP's uniformity and the detector's non-uniformity. Therefore, it is necessary to have available an appropriate flat region scan for any given operating parameters.

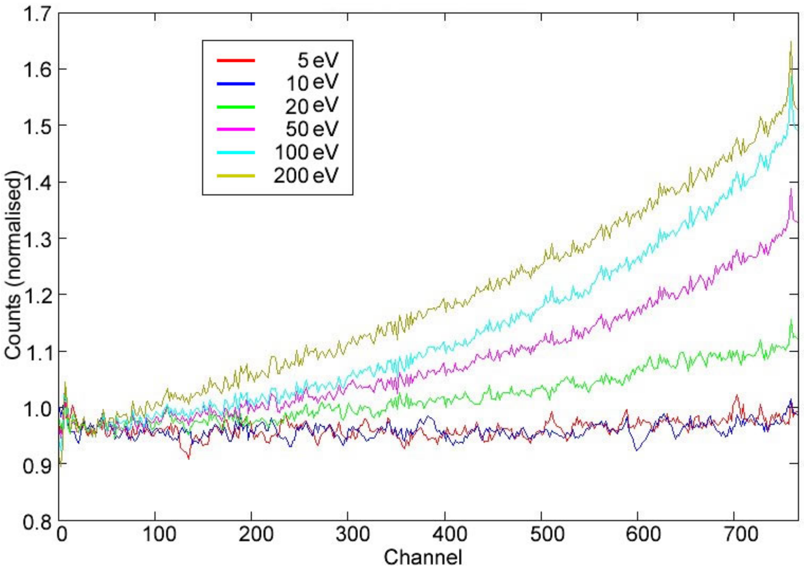

Figure 4.3: Flat region scans taken at different analyser pass energies

### 4.1.2 Decimation

Splitting the measured spectrum into groups of, say, eight points and summing each point in each group results in a spectrum with fewer points and with diminished effects of non-uniformity. In this situation, this strategy has been seldom utilised as it does not represent a very efficient use of the available data, giving a further loss of resolution on top of that loss incurred due to pulse spreading.

$$CS_i = \sum_{j=i\cdot df}^{(i+1)\cdot df} MS_j \tag{4.2}$$

### 4.1.3 Weaving

Only applicable to scanned spectra. As the retard potential of the analyser is scanned, subsequent measured spectra are overlapping sections of the entire

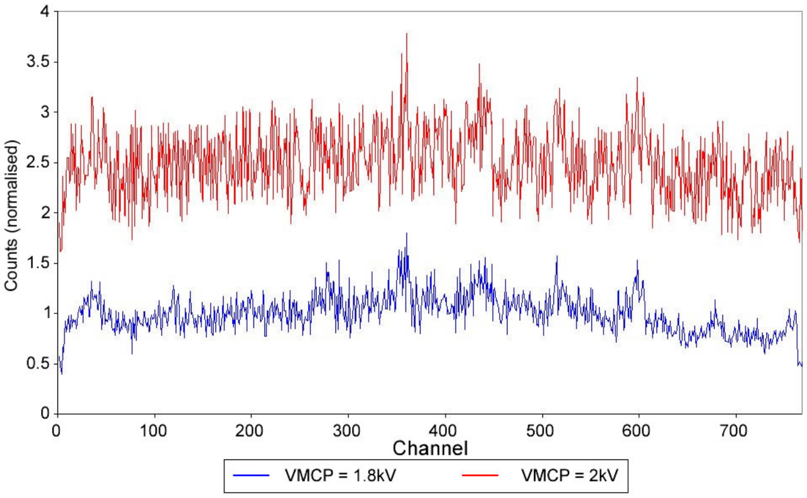

Figure 4.4: Flat region scans taken at different MCP voltages

spectrum under investigation. These spectra can then be combined by translating each one along the energy scale by an appropriate amount and summing all the overlapped spectra. To do this, the distance in pixels that the spectrum is translated along the array as retard potential is varied must be measured. This can be done by scanning a single peak across the array, and fitting an appropriate function (generally, this has been a gaussian) to each individual spectrum. This enables the amount by which consecutive scans must be shifted to be found. Therefore the peak position, in pixels, can be found for each spectrum at which the retard potential is known (figure 4.6), therefore, the pixels per eV can be found.

By multiplying this value by the step in retard potential between each step, the number of pixels each spectrum needs to be translated by can be found. Once all the spectra have been offset by the required amount, each column is averaged, to give a single spectrum.

As previously discussed in section 4.1.3, weaving scanned spectra gives a

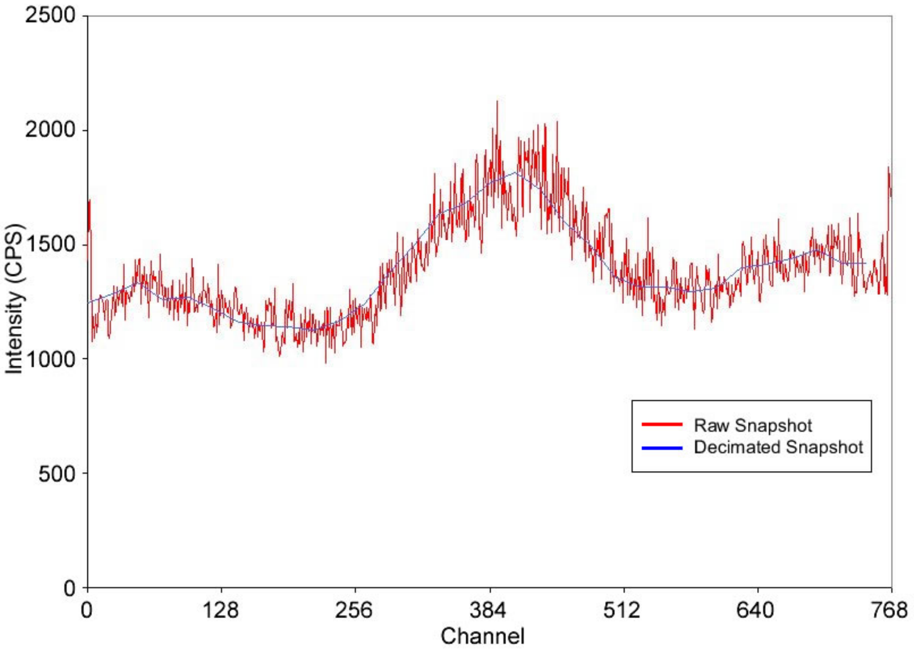

Figure 4.5: Decimated data

spectrum that is at least partially corrected for non-uniformity as each pixel contributes to every point on the resulting spectrum. However, when taking a single or multiple snapshots, this is not an available strategy due to the retard potential remaining constant. However, by taking a scanned spectrum of a region of interest in addition to the experimental snapshots, some of the benefits of weaving can be applied to the snapshot. This scanned spectrum must be of the same sample, and use the same operational parameters as the intended snapshot. Of equal importance is that the range and step of the retard potential is such that the individual spectrum halfway through the scan is of the same retard potential as the intended snapshot.

Now, by selecting from the unwoven spectra the individual snapshot that has KE equal to the experimental snapshot and comparing that reference spec-

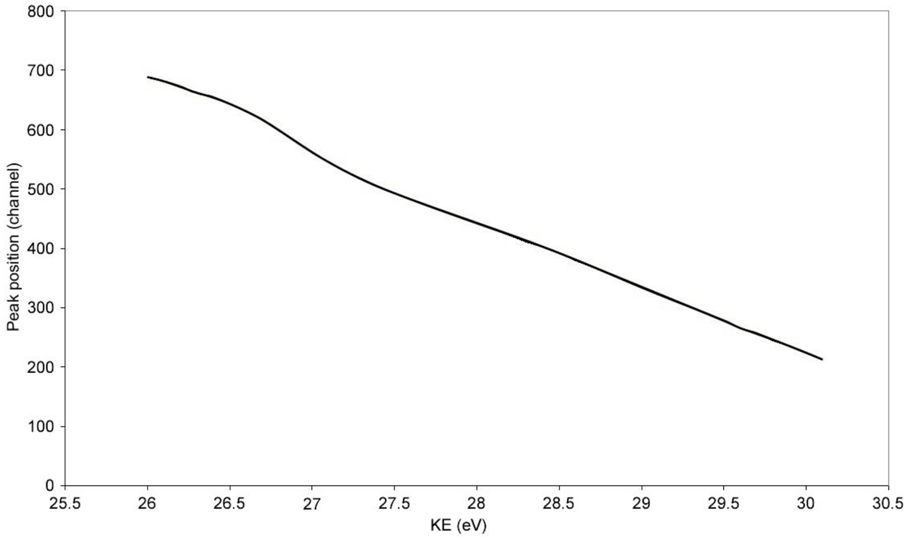

Figure 4.6: Peak position as retard potential is scanned

trum to the corresponding section of the woven spectrum, information on both non-uniformity and lineshape distortions becomes available. By dividing the reference scan with the section of woven spectrum, and splitting the resultant vector into high- and low-frequency components as in figure 4.8, the information on non-uniformity and lineshape distortions can be obtained separately.

Selecting the weave correction forces the operation of an additional module to analyse the swept data file to find the pixel offset per unit change in retard potential.

When the weave correction is utilised, the corrections available to apply to the snapshot data can also be applied to the woven spectrum, and the reference spectrum, should it be so desired.

$$CS_i = \sum_j MS_j(i,j) \tag{4.3}$$

In figure 4.9, it can be seen that the spectrum obtained by weaving the in-

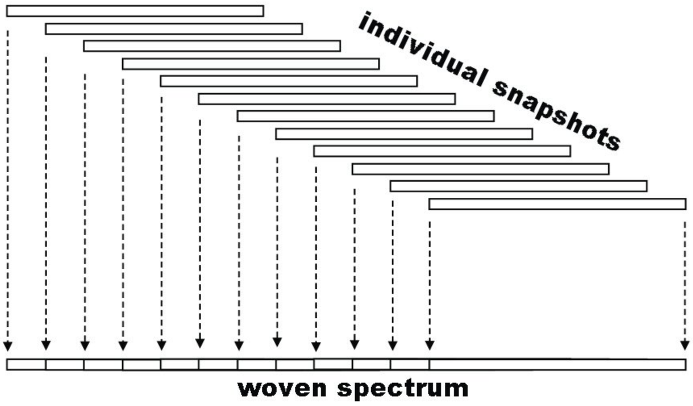

Figure 4.7: Weaving individual snapshots to give wide spectrum

dividual snapshots (of which three are pictured) has greatly reduced noise. The increase in noise towards the extremes of the spectrum are caused by contributions from increasingly fewer snapshots.

### 4.1.4 Point spread function correction

The methods outlined above all share a particular flaw: no attempt is made to recover resolution lost due to pulse spreading in the array module. Given a representation of the profile of the pulse spreading, it is possible that the resolution could be restored somewhat by compensating for this PSF from the measured spectrum as well as performing one of the preceeding correction methods.

This correction can be performed in a number of ways, of varying complexity and accuracy. Key to all of these methods is knowledge of the pulse size distribution, obtained via a speckling experiment as described in section 3.3.2.

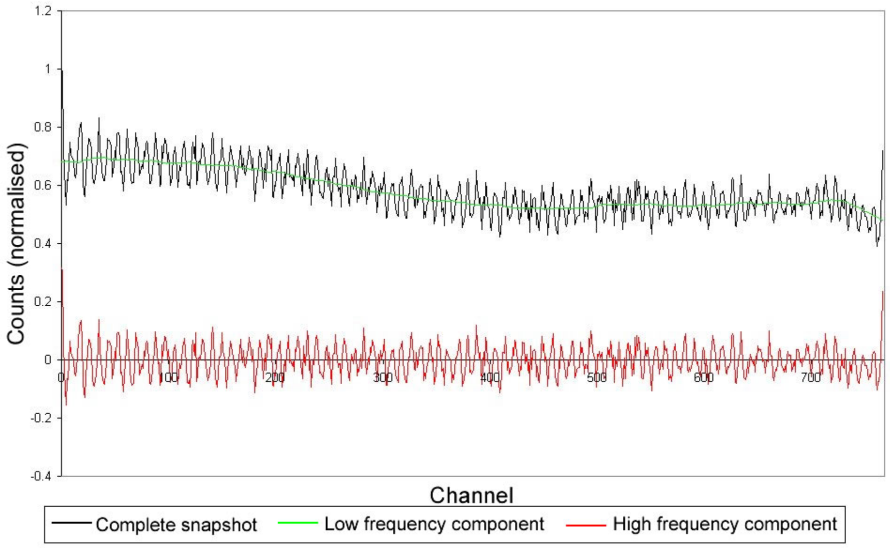

Figure 4.8: Snapshot split into high and low spatial frequency components

### Linear Correction

Whilst conceptually simple and easy to implement, simple vector correction fails to take account of the fact that pulse spreading between the first and second MCPs and between the second MCP and the readout device results in a single event registering on a number of channels, resulting in an artificial increase in measured intensity: given a mean pulse size, $P$, each individual event will trigger $P$ channels. Therefore, by multiplying each channel's count by $1/P$, this over-reading can be compensated for. This simple correction can easily be combined with any of the previously mentioned correction algorithms to give an improved approximation of the incident spectrum. This approach will not increase resolution, or improve the signal-to-noise ratio further, but will give a more accurate number of counts.

The non-recovery of lost resolution may not in all instances be a great problem - if a spectrum's narrowest feature is significantly wider than the mean pulse

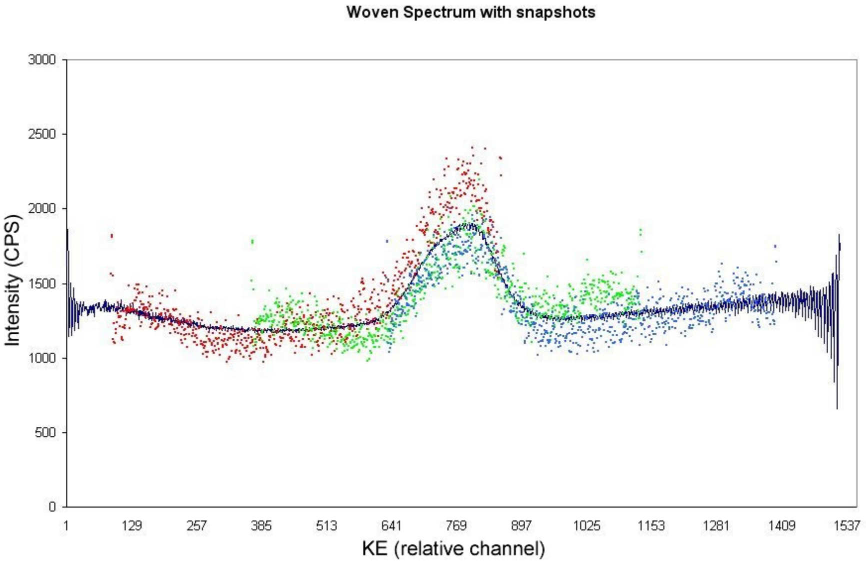

Figure 4.9: Individual snapshots with completed weave

size, it may not be considered vital to correct for the lost resolution.

$$CS_i = \frac{MS_i}{NFF_i \cdot \overline{ES}} \tag{4.4}$$

### Deconvolution of mean pulse profile

Using the speckle data, the mean pulse spread profile can be calculated. Now, given that, barring any other aberrations, the measured spectrum can be arrived at by convolving the incident spectrum with this mean pulse profile. Therefore, deconvolving the mean pulse profile from the measured spectrum will give the incident spectrum.

$$CS_i = IFFT\left[\frac{FFT(MS)}{FFT(PSF)}\right] \tag{4.5}$$

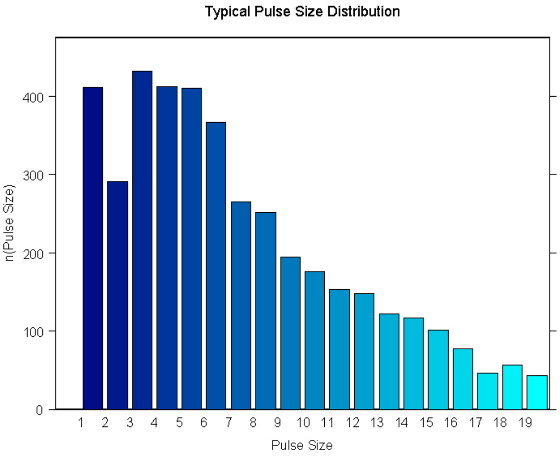

Figure 4.10: Pulse Size Distribution for Entire Array

### Forward Deconvolution

This well-documented technique [6] can be implemented by representing the incident spectrum as a vector, $S_I$, and the measured spectrum as another vector, $S_M$. The aberrations introduced by the system can be modelled as multiplication by B, a square matrix.

$$S_M = S_I \cdot B \tag{4.6}$$

Now, given knowledge of B, it should be possible to calculate B's inverse matrix, such that.

$$S_I = S_M \cdot B^{-1}$$

So that multiplying the measured spectrum with $B^{-1}$ gives the incident spectrum. However, the matrix B is found to be very close to being singular - it's determinant is very close to zero. Therefore, even the slightest error in B leads to a very large error in $B^{-1}$, and hence in any recovered spectrum. Because of this, it becomes necessary to utilise forward deconvolution [24]. Revisiting equation 4.6, it can be seen that by starting with an estimate of the incident spectrum, $GIS$ and multiplying it by the matrix B, the result, $GMS$ will be equivalent to the measured spectrum obtained if the guess spectrum was equivalent to the actual incident spectrum. Thus, by comparing $GMS$ with $MS$ the actual measured spectrum, it can be seen how accurate an estimate of the actual incident spectrum $GIS$ actually is. An iterative technique can then be used, so that the guess spectrum gets modified progressively closer to the actual incident spectrum. The comparison method used here is a simple $\chi^2$ test:

$$\chi^2 = \sum_{i=1}^{n} \left( \frac{(MS - A \cdot GIS)^2}{A \cdot GIS} \right)$$

By using a suitable numerical technique to modify the guess spectrum to minimise the value of $\chi^2$, the guess spectrum becomes a more accurate representation of the incident spectrum. This relies, of course, on the matrix A being as accurate a model of the arrays performance as possible.

A further development of this strategy is to introduce a term that represents the entropy of the guess spectrum - this gives an indication of how much information is present in the guess spectrum and works to prevent convergence onto a flat zero spectrum. The entropy of a spectrum is given by:

$$H(S'_I) = -\sum_{i=1}^{n} \left( \frac{S'_{I_i}}{\sum_{i=1}^{n} S'_{I_i}} \log \left( \frac{S'_{I_i}}{\sum_{i=1}^{n} S'_{I_i}} \right) \right)$$

This is used by combining this entropy term with the $\chi^2$ test:

$$H(S'_I) - \lambda\chi^2 = maximum$$

Here $\lambda$ is a constant introduced to ensure that the entropy term and the $chi^2$ term are of roughly of the same order of magnitude.

### 4.1.5 Electron Optics Correction

Data required: two flat region scans, one taken at low pass energy (10 or 20eV) and one taken at the experimental pass energy Flat region scan comparison. Two flat region scans are taken, one at a pass energy low enough for analyser and lens aberrations to be considered insignificant, typically around 10-20eV, and the other at the pass energy at which the snapshot is to be taken (typically 100-200eV). Comparing the two spectra gives an indication of the distortion in a flat field, and by running the correction vector through a low-pass filter, any artefacts due to varying non-uniformity between the high and low pass energy spectra can be removed.

### 4.1.6 Linearity correction

Data required: two spectra, taken at high and low x-ray fluxes respectively As count rate increases, the ability of the MCPs to recharge between pulse becomes impaired. As a result, the count rate begins to drop off, resulting in erroneously lower counts. To counter this requires two spectra - one taken at a low x-ray flux, and one taken at a higher electron flux. Now, by dividing each spectrum by the corresponding x-ray flux used, and plotting corresponding points against each other should give, for an ideal system, a straight line, where d(Fl)/d(Fh) is equal to unity. However, in reality, the lower end of the line is somewhat broadened, due to signal noise at low count rates, and towards the high end, d(Fl)/d(Fh) begins to decrease. This decrease is the effect of non-linearity, caused by the MCPs becoming saturated at high count rates and being unable to fully recharge between events. Next, by fitting a curve (either a polynomial, or exponential) to this line, a correction for non-uniformity can be arrived at.

This correction can then be applied to measured spectra.

## 4.2 Correction Order

The most intuitive order in which to apply corrections is the reverse order in which they occurred in the system; the last aberration in the system is the non-uniformity of the readout device, and so this should be corrected for first when manipulating the measured spectrum.

However, this is not always possible - the information obtained on non-uniformity includes contributions from the the readout device and from the MCP stack. Similarly, the pulse spreading information acquired via speckling experiments yields the effects of the inter-MCP spreading combined with the spreading that takes place between the second MCP and the readout device. Should it become possible to measure the individual non-uniformities of the two MCPs and readout device, and to independently measure the pulse spreading between the two MCPs and between the second MCP and the readout device, then no compromise in ordering the corrections would be necessary.

## 4.3 Evaluation of Strategies

In order to choose which strategy, or combination of strategies, is of most use, some way of objectively assessing it's efficacy must be used.

### 4.3.1 Common Operations

When evaluating the usefulness of correction algorithms, there are several steps that are common to most, if not all, assesments.

### Analysis of a single spectrum

Spectra can be broken down, using Fourier decomposition, into components representing each spatial frequency present in the spectrum. Analysis of which frequencies are present, and to what extent can reveal information on the quality of the spectrum. Corrected spectra will often contain amounts of high frequency noise. By examination of a spectrum's frequency distribution, obtained by Fourier transform, the amount of high-frequency components in the spectrum can be seen, and from that, the amount of unwelcome noise can be inferred - the majority of real features will have spatial frequencies significantly greater than that of the array. However, certain real artefacts are variations upon a step function, which will carry a high-frequency component. By observation of the spectrum, it can often be seen whether the high frequency component is due to a step in the signal, or noise. Therefore care must be taken when examining the frequency distribution to ascertain whether observed high frequency components are due to signal or noise.

Figure 4.11 shows the power specta of a snapshot before and after it has been corrected. It can be seen that higher frequency signals, corresponding to noise are uniformly lower, showing an improved signal/noise ratio.

### Comparison of Two Spectra

Often, a snapshot needs to be compared against another, reference snapshot. This can be done in a number of ways. One way is a $\chi^2$ test:

$$\chi'^2 = \sum_{i=0}^{n} \frac{(Sref_i - S_i)^2}{S_i} \tag{4.7}$$

where Sref is the reference snapshot and S is the snapshot of interest.

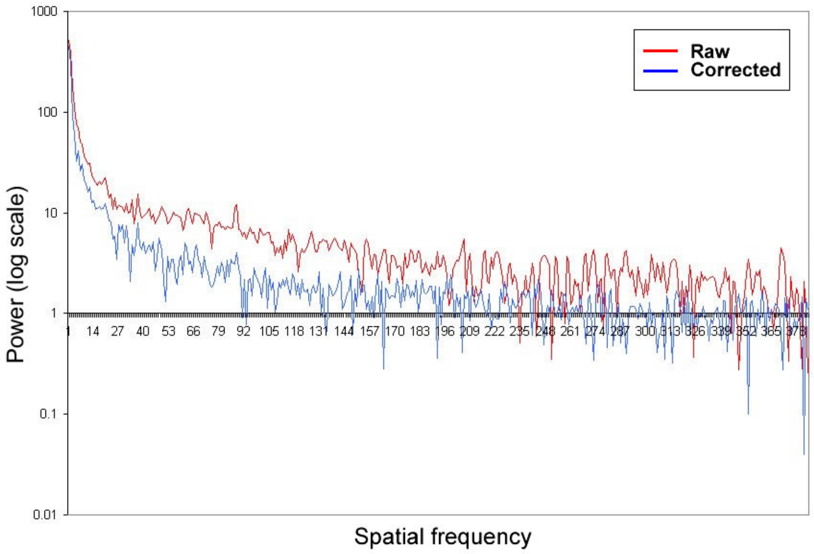

Figure 4.11: Power spectra of a corrected and uncorrected snapshot

**Measurement of Information**

To guard against the possibility of a correction method returning a useless result, for example, a spectrum where each point is zero, the entropy of the returned spectrum can be checked, as outlined in section 4.1.4.

### 4.3.2 Consistency

An ideal correction algorithm will correct all non-uniformities in the system to an extent that when corrected, a feature will look the same, independantly of it's location on the detector array. So, when a feature is being scanned across the array, once the individual snapshots have been corrected, this feature should be able to be superimposed with itself for each snapshot taken, once translated by a suitable amount along the energy axis.

Once aligned, the feature can be averaged for each snapshot, and the stan-

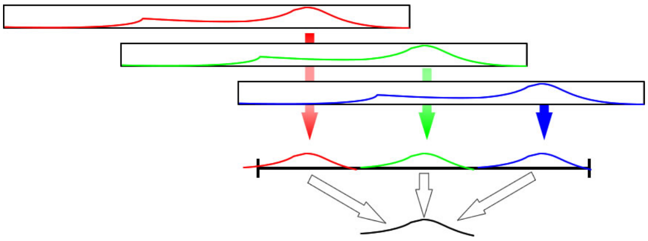

Figure 4.12: A snapshot of a feature, when corrected, should be identical to other snapshots where the same feature is located on a different part of the array

dard deviation for each point will be representative of the variation between individual snapshots. If the snapshots are perfectly corrected, this standard deviation will be close to zero (errors in the translation along the energy axis will affect this measurement despite not being directly related to the performance of the correction algorithm)

### 4.3.3 Accuracy

Whilst the previous test is a measure of the consistency of the corrected result, if the corrected result is consistently wrong, this is of no use. For example, if the correction algoritm consistently produced a flat, uniform signal, then the consistency test would indicate, correctly, that all the snapshots had been corrected identically. This problem could be avoided, either with an “eyeball” stage, where corrected spectra are visually checked to be useful, non-trivial results. However, a numerical, rather than subjective, test would reveal the usefulness of a corrected spectrum. This can be done by comparing snapshots with a known, accurate spectrum. A spectrum acquired from a single channel as the incident spectrum is scanned accross the array will be free of non-uniformities. If these indiviual single-channel spectra are summed, then the resulting spectrum will be or comparable quality to those taken with a channeltron. If this summed spectrum is used as an authorative spectrum, then comparing corrected snapshots against it will give an indication of the quality of the corrected data.

### 4.3.4 Reversing Forward Deconvolution

As previously discussed, the matrix A represents the transformation that the system imposes upon the incident spectra to result in the measured spectra. As discussed in [6], if this matrix is applied to a corrected or recovered spectrum, the given re-distorted spectrum can be compared with the measured spectrum. This method of assessing correction strategies relies upon the accuracy of the matrix A. Additionally, if the matrix A used is also used for performing the forward deconvolution recovery, it cannot be then used for this assesment as this would be a circular comparison.

# Chapter 5

# Real Time XPS

The purpose of the experiment described here was to observe the behaviour of a diamond $C1^s$ peak in real time as the sample was heated and cooled. The sample used was a diamond (111) surface, initially with a 1×1 hydrogen-terminated surface. Previous studies [7] have shown the $C1^s$ peak shifting as the surface reconfigures to a 2×1 clean surface. Until the development of real-time XPS, this transition had not been witnessed in real time [22].

## 5.1 Experiment Configuration

In addition to the standard REES setup, a sample heater was used to heat the diamond sample as spectra were taken in real time. This heater was controlled by the same PC as the detector array and electron optics, allowing the heater to be given a specific program of heating to a set temperature, holding that temperature, and the cooling at a specified rate. X-rays were produced by the MgK$\alpha$ source.

The system was set to take snapshots of the $C1^s$ peak. The power supply profile for the heater was set so that there was time to take a number of snapshots before the heating and cooling cycle began. As snapshots were taken in real time, it was possible to monitor the effects of heating upon the position, height and quality of the peak.

## 5.2 Results

As an overview, the watched peak can be seen in figures 5.1 and 5.2.

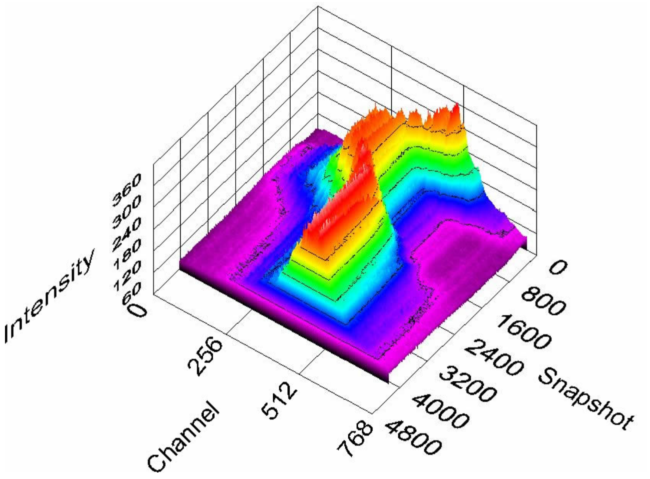

Figure 5.1: Uncorrected realtime data

For analytical purposes, it is more useful to show the peak's position and height separately, as in figure 5.3

From this, it can be seen that heating increases the peak amplitude - as the surface hydrogen is desorbed, the underlying diamond's spectrum is less attenuated. The peak shift due to surface reconstruction can be seen. [7]

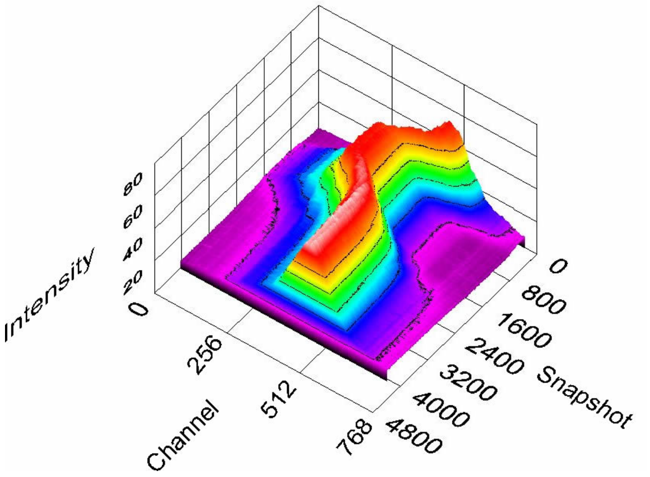

Figure 5.2: Corrected realtime data

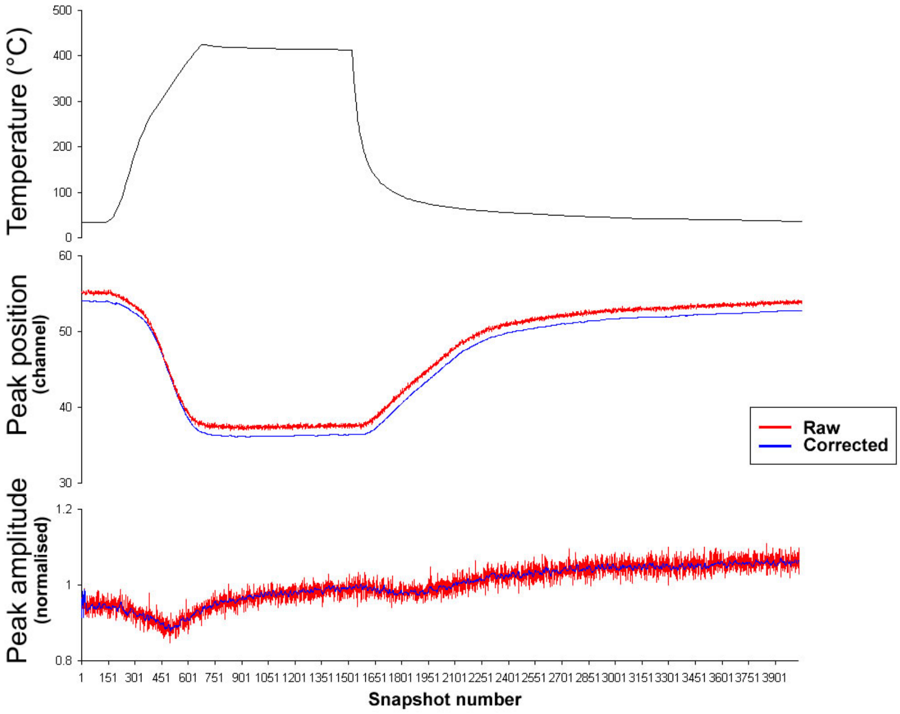

Figure 5.3: Realtime peak amplitude

# Chapter 6

# Conclusions

## 6.1 Effect of applying corrections

From the results presented in 5.2, it can be seen that the correction algorithm used here can increase the signal/noise ratio in both individual snapshots, and in peak-tracking data from real-time experiments. However, it was found that the most effective correction method - forward deconvolution - remains prohibitively expensive in terms of computing power for real-time applications; where thousands of individual snapshots are concerned, the extra detail obtainable is not significant when compared to the time taken. However, when only a few snapshots need correcting, forward deconvolution does provide the best results, and as computing power increases, will become more viable as a correction strategy for all data.

## 6.2 Further and outstanding work

The work presented here has fallen far short of it's intended scope. The original intention to develop a universal correction algorithm that has been rigorously characterised has not been realised. Rather, this work may serve as an indicator of a number of avenues of investigation.

# References

[1] P.Grunberg W.Zinn A.Fuss, S.Demokritov. *J.Magn.Mat.*, 103:L221, 1992.

[2] D.C Anacker and J.L. Erskine. Analysis of microchannel plate response in relation to pulsed laser time-of-flight photoemission spectroscopy. *Review of Scientific Instruments*, 62(5):1246–1255, 1991.

[3] O.H.W. Siegmund A.S. Tremsin. Spatial distribution of electron cloud footprints from microchannel plates: Measurements and modeling. *Rev. Sci. Inst*, 70(8):3282–3288, August 1999.

[4] O.H.W. Siegmund et al A.S. Tremsin. Electronic and optical moiré interface with microchannel plates: artifacts and benefits. *Applied Optics*, 38(11):2240–2248, April 1999.

[5] K. Birkinshaw. Spectrum recovery from discrete detector arrays - correction for nonuniformity. *Int. J. Mass Spec.*, 181:159–165, 1998.

[6] K. Birkinshaw. Deconvolution of mass spectra measured with a non-uniform detector array to give accurate ion abundances. *Journal of Mass Spectrometry*, 38(38):206–210, January 2003.

[7] A. Bushell. *The Integration and Use of a Multi-channel Detector for Electron Spectroscopy.* PhD thesis, UWA, 2004.

[8] Evelyn Sokolowski Carl Nordling and Kai Siegbahn. Precision method for obtaining absolute values of atomic binding energies. *Phys. Rev.*, 105:1676–1677, 1957.

[9] T. Chase D. Langstaff. A multichannel detector with 768 pixels developed for electron spectroscopy. *Nuclear Instruments and Methods B*, 573:169–171, April 2007.

[10] David A. Dahl. Simion for the personal computer in reflection. *International Journal of Mass Spectrometry*, 200:3–25, 2000.

[11] A. Einstein. On a heuristic viewpoint concerning the production and transformation of light. *Annalen der Physik*, 17:132–148, 1905.

[12] C. Martin et al. Wedge-and-strip anodes for centroid-finding position-sensitive photon and particle detectors. *Rev. Sci. Inst*, 52(7):1067, July 1981.

[13] D.P. Langstaff et al. A new ion detector array and digital-signal-processor-based interface. *Meas. Sci. Technol*, 5:389–393, 1994.

[14] D.P. Langstaff et al. A fully integrated multi-channel detector for electron spectroscopy. *Nuc Inst Meth Phys B*, 238:219–223, 2005.

[15] S. Hüfner F. Reinert. Photoemission spectroscopy - from early days to recent applications. *New Journal of Physics*, 7(97):All, April 2005.

[16] G.E.Vibrans. Computation of the spreading of an electron beam under acceleration and space-charge repulsion. *MIT*, 1963.

[17] J.E. Lees et al. G.W. Fraser, M.T. Pain. The operation of microchannel plates at high count rates. *Nucl. Inst. Meth. A*, 306:247–260, 1991.

[18] J.F. Pearson G.W. Fraser and J.E. Lees. Dark noise in microchannel plate x-ray detectors. *Nucl. Inst. Meth. A*, 254:447–462, 1987.

[19] J.F. Pearson G.W. Fraser and J.E. Lees. Microchannel plate operation at high count rates - further-studies. *Nucl. Inst. Meth. A*, 327(2-3):328–336, 1993.

[20] HKUST. Introduction to x-ray photoelectron spectroscopy.

[21] JB Hudson. *Surface Science*. Butterworth-Heinmann, 1992.

[22] J. Ristein J. B. Cui and L. Ley. *Phys. Rev. Lett.*, 81:429, 1998.

[23] D.P. Langstaff. An mcp-based detector array with integrated electronics. *Int. J. Mass Spec.*, 215:1–12, 2002.

[24] Dinesh J. Narayan. *The Investigation of Non-Uniformity in Discrete Detector Arrays*. PhD thesis, UWA, 2002.

[25] Kai Siegbahn. Electron spectroscopy for atoms, molecules, and condensed matter. *Science*, 217(4555):111–121, July 1982.

[26] SPECS. *UVS 300 manual*.

[27] SPECS. *UVS XR3E2 Manual*.

[28] Thermo VG Scientific. *CLAM4 Analyser Systems Operating Manual*, 4 edition, 03 2001.

[29] W. L. Yang et al. X. J. Zhou, B. Wannberg. Space charge effect and mirror charge effect in photoemission spectroscopy. *Journal of Electron Spectroscopy and Related Phenomena*, 142(1):27–38, 2004.

[30] T.J.M Zouros and E.P. Benia. The hemispherical deflector analyser revisited. i. motion in the ideal 1/r potential, generalized entry conditions, kepler orbits and spectrometer basic equation. *J. Elec. Spec.*, 125:221–248, 2002.